Hexokinase regulates Mondo-mediated longevity via the PPP and organellar dynamics

Raymond Laboy[1,2], Marjana Ndoci[1], Maximilian Vonolfen[1,2], Eugen Ballhysa[1,2], Ilian Atanassov[1], Adam Antebi[1,2*]

1 Department of Molecular Genetics of Ageing, Max Planck Institute for Biology of Ageing, Cologne, Germany

2 Cologne Excellence Cluster on Cellular Stress Responses in Aging-Associated Diseases (CECAD), University of Cologne, Germany

*For correspondence: antebi@age.mpg.de

Abstract

The transcriptional complex Mondo/Max-like, MML-1/MXL-2, acts as a convergent transcriptional regulatory output of multiple longevity pathways in *Caenorhabditis elegans*. These transcription factors coordinate nutrient sensing with carbohydrate and lipid metabolism across the evolutionary spectrum. While most studies have focused on the downstream outputs, little is known about the upstream inputs that regulate these transcription factors in a live organism. Here, we found that knockdown of various glucose metabolic enzymes decreases MML-1 localization in the nucleus and identified two hexokinase isozymes, *hxk-1* and *hxk-2,* as the most vigorous regulators of MML-1 function. Upon hexokinase knockdown, MML-1 redistributes to mitochondria and lipid droplets (LD) and concomitantly, transcriptional targets are downregulated and germline longevity is abolished. Further, we found that *hxk-1* regulates MML-1 through mitochondrial β-oxidation, while *hxk-2* regulates MML-1 through modulating the pentose phosphate pathway (PPP) and its coordinated association with lipid droplets. Similarly, inhibition of the PPP rescues mammalian MondoA nuclear translocation and transcriptional function upon starvation. These studies reveal how metabolic signals and organellar communication regulate a key convergent metabolic transcription factor to promote longevity.

Key words: MondoA/ChREBP, MML-1, lipid droplet, metabolism, aging, transcription

Introduction

Aging is a complex multifactorial process associated with the decline of organismal homeostasis and an increased risk of age-related diseases. One key aspect of aging is the dysregulation of gene expression and metabolism (Fischer et al., 2022). Many transcription factors that regulate metabolic pathways have been shown to control lifespan in the evolutionary spectrum (Clancy et al., 2001; Green et al., 2021; Lapierre et al., 2013; Selman et al., 2008; Wang et al., 2008). Changes in the activity of specific transcription factors have been shown to impact gene expression patterns and alter metabolic processes, leading to a decline in cellular function and increased risk of age-related diseases (Benhamed et al., 2012; Carroll et al., 2015; Denechaud et al., 2008; Du & Zheng, 2021; Tong et al., 2009). Thus, understanding the interplay between metabolism and transcriptional regulation is crucial for gaining insight into the mechanisms underlying aging and developing novel strategies for promoting healthy aging and reducing the risk of age-related diseases.

MondoA and ChREBP are paralogue transcription factors that work in heterodimeric complexes with Mlx and have been identified as key regulators of glucose metabolism and energy homeostasis. These transcription factors recognize and bind hexanucleotide tandem sequences (CANNTG) in the promoter regions called Enhancer box (E-box) sequences (Massari & Murre, 2000) of various genes involved in glucose uptake, utilization, and storage (Billin et al., 2000; Cha-Molstad et al., 2009; Sans et al., 2006; Stoltzman et al., 2008; Yamashita et al., 2001). In addition to their role in glucose metabolism, MondoA/ChREBP have also been shown to play a role in the regulation of lipid metabolism and cellular stress response (Iizuka et al., 2006; Ishii et al., 2004; Ma et al., 2006). Studies have suggested that changes in MondoA/ChREBP activity with age may contribute to age-related metabolic dysfunction, leading to a decline in glucose tolerance and increased risk of type 2 diabetes and obesity (Ghasemi et al., 2015; Iizuka et al., 2006; Richards et al., 2017; Yamamoto-Imoto et al., 2022).

In *Caenorhabditis elegans,* the transcriptional complex formed by MML-1/MXL-2 is part of an integrated helix-loop-helix (HLH) network required for lifespan extension in diverse longevity pathways (Johnson et al., 2014; Nakamura et al., 2016), although it is still unknown how these transcription factors integrate multiple upstream signals to regulate lifespan. In this work, we describe how metabolic inputs regulate MML-1 subcellular localization and function. We found that HXK-1 and HXK-2 regulate MML-1 cellular distribution and are required for germline longevity through the regulation of mitochondrial β-oxidation and the pentose

67 phosphate pathway (PPP), respectively. Moreover, inhibition of MML-1 nuclear translocation
68 results in the relocalization of this transcription factor to mitochondria associated with lipid
69 droplets (LD). This study provides key insights into how glucose and lipid metabolism directly
70 impact transcriptional regulation and aging.
71
72 **Results**
73 *Hexokinases are required for MML-1 subcellular localization and germline-mediated*
74 *longevity*
75 MondoA reportedly responds to glucose 6-phosphate (G6P) and other hexose
76 phosphate sugars in cultured cells by translocating to the nucleus and regulating the expression
77 of its downstream targets (Stoltzman et al., 2008, 2011). Nevertheless, little is known about the
78 regulation of MondoA in an organism-wide setting, and most subsequent work has focused on
79 the molecular mechanisms downstream of this transcription factor. Hence, we decided to
80 investigate how MML-1 is regulated by upstream glucose metabolism in *C. elegans*. To address
81 this, we performed a targeted RNA interference (RNAi)-based screen on genes encoding
82 enzymes involved in glucose metabolism. Overall, we found a preponderance of decreased
83 intestinal MML-1 nuclear localization when knocking down such genes (**Figure 1A-B,**
84 **Supplementary Table S1**). Knockdown of most of the enzymes involved in glycolysis as well
85 as the pyruvate dehydrogenase complex, which links glycolysis to the tricarboxylic acid (TCA)
86 cycle via acetyl-CoA, decreased accumulation of nuclear MML-1 (**Supplementary Table S1**).
87 Interestingly, whereas most enzymes in the TCA cycle also decreased nuclear MML-1,
88 inhibition of the oxoglutarate dehydrogenase complex (OGDC) subunits *ogdh-1* and *dld-1* and
89 the succinyl-CoA synthase (SCS) *suca-1* and *sucg-1* subunits increased MML-1 nuclear
90 localization. We also observed that knockdown of enzymes involved in the oxidative and
91 non-oxidative branches of the pentose phosphate pathway (PPP), phosphogluconate
92 dehydrogenase (PGDH) *T25B9.9* and transketolase (TKT) *tkt-1* genes, respectively, triggered
93 a strong increase in MML-1 nuclear accumulation (**Figure 1A-B**). Taken together, these data
94 suggest that overall changes in glucose metabolism regulate MML-1 and that this transcription
95 factor may sense the divergence of G6P to different branches of this pathway.
96 Our screen revealed that hexokinase knockdown had the most potent effect in
97 decreasing MML-1 nuclear localization. This enzyme is involved in the first step of glucose
98 metabolism, phosphorylating glucose to G6P, and is a critical mediator of cellular metabolism.
99 Among the three *C. elegans* hexokinase genes, *hxk-1* and *hxk-2* more strongly affected MML-1
100 nuclear localization in two independent MML-1::GFP reporter strains (**Figure 1B,**

101 **Supplementary Figure 1A**). To test whether the phosphotransferase activity of hexokinase is
102 responsible for regulating MML-1 nuclear localization, we used two drugs to inhibit
103 hexokinases pharmacologically. 3-Bromopyruvate (3-BrP) is an alkylating agent and HKII
104 inhibitor, and 2-deoxy-glucose (2-DG) is an analog of glucose phosphorylated to 2-DG6P
105 which cannot be further metabolized, thus inhibiting hexokinase function. Supplementation of
106 both drugs significantly decreased MML-1 nuclear localization compared to control
107 (**Supplementary Figure 1B-C**), indicating that hexokinase activity is driving MML-1 nuclear
108 translocation. We also tested the specificity of RNAi knockdown by using strains where the
109 three endogenous hexokinase loci were tagged with mKate2. We used these strains to evaluate
110 the protein levels by Western blot and found that each RNAi was specific to each isozyme
111 (**Supplementary Figure D-E**). As glycolysis is essential during development, we measured
112 the size (area and length) of worms fed with hexokinase RNAi egg-on. *hxk-1i* and *hxk-2i*
113 displayed no significant change in worm growth, while *hxk-3i* treated animals were somewhat
114 smaller (**Supplementary Figure 1F-G**). To determine if our observations were due to a change
115 in food intake, we counted pharyngeal pumping rate but found no significant difference
116 compared to the control (**Supplementary Figure 1H**), nor did we see an effect on worm
117 motility compared to control (**Supplementary Figure 1I**). Moreover, hexokinase knockdown
118 did not affect the steady-state levels of *mml-1* mRNA (**Supplementary Figure 1J**). Taken
119 together, these data indicate that there is no RNAi cross-reactivity among the hexokinase
120 isozymes and that the effects on MML-1 nuclear localization are not due to a decrease in food
121 consumption or developmental phenotype.
122 MML-1 works in a transcriptional complex with MXL-2, and previous studies have
123 demonstrated that MML-1/MXL-2 are required for lifespan extension in multiple longevity
124 pathways, including germline-less *glp-1(e2141)* mutant (Nakamura et al., 2016). Hence, we
125 tested whether hexokinases influenced MML-1 subcellular localization in this longevity model.
126 As expected, MML-1 nuclear localization was increased in *glp-1(e2141)* as reported previously
127 (Nakamura et al., 2016), and upon *hxk-1* and *hxk-2* knockdown, MML-1 nuclear localization
128 was abolished in *glp-1(e2141)* mutants (**Figure 1C-D**). Changes in MML-1 nuclear
129 localization would be expected to modulate its transcriptional activity. To test this idea, we
130 next analyzed the expression of downstream targets reportedly linked to the gonadal longevity
131 (Nakamura et al., 2016). We observed decreased expression of *mdl-1*, *lgg-2*, *swt-1*, and *fat-5*
132 under *hxk-1i* and *hxk-2i,* but not under *hkx-3i* (**Figure 1E, Supplementary Figure 1K**),
133 consistent with decreased MML-1 transcriptional activity. Since hexokinase knockdown
134 decreases MML-1 nuclear localization in the *glp-1(e2141)* longevity model, we reasoned that

135 the lifespan might also be abolished. Accordingly, *hxk-1i* and *hxk-2i* significantly decreased
136 *glp-1(e2141)* but did not significantly affect wildtype lifespan (**Figure 1F**). Collectively, these
137 data indicate that hexokinases are upstream regulators of MML-1 nuclear localization and
138 transcriptional function in *C. elegans*.
139
140 *C. elegans hexokinases are differentially expressed*
141 Mammals harbor four hexokinases that differ in tissue expression, subcellular
142 localization, and affinity to glucose and G6P. However, knowledge of the nematode's isozymes
143 is limited. We used the hexokinase tagged with mKate2 strains to investigate the tissue-specific
144 expression and subcellular localization of the different isozymes by confocal microscopy. We
145 found that HXK-1 was expressed in the cytosol of neurons, pharynx, gonadal sheath, and
146 coelomocytes (**Figure 2A**). HXK-2 had a reticular expression in neurons, muscle, intestine,
147 and hypodermis (**Figure 2B**). HXK-3 signal was diffused and highly expressed in the pharynx,
148 muscle, hypodermis, and intestine (**Supplementary Figure 2A**).
149 Human HKI and HKII have been shown to bind reversibly to the mitochondria (Sui &
150 Wilson, 1997). Binding depends on an intrinsic hydrophobic N-terminal sequence critical for
151 inserting into the outer mitochondrial membrane (Pastorino et al., 2002). Due to the reticular
152 expression pattern, HXK-2 was a plausible candidate to be mitochondrially localized. To
153 corroborate this idea, we crossed the HXK-2::mKate2 strain with a mitochondrial reporter that
154 expresses GFP with a mitochondrial targeting sequence under the body wall muscle promoter
155 *myo-3.* Indeed, we observed that full-length HXK-2 strongly co-localized with mitochondria
156 (**Figure 2C**). We also generated an HXK-2 mutant that lacks the first ten amino acids after the
157 initiator methionine (d10 HXK-2) and found that mitochondrial localization was abolished
158 entirely (**Figure 2C**). In summary, we found that hexokinases are differentially expressed in
159 *C. elegans* and identified HXK-2 as the worm mitochondrial hexokinase.
160
161 *Hexokinase knockdown increases MML-1 mitochondrial localization*
162 Since we observed that *mml-1* mRNA levels were unaffected by *hxk* knockdown and
163 saw a decrease in MML-1 nuclear localization upon hexokinase knockdown, we wondered
164 whether MML-1 might re-localize to another subcellular compartment. First, we crossed the
165 MML-1::GFP reporter strain with two compartmental markers and examined colocalization by
166 confocal microscopy. We looked at the lysosome/endosome reporter strain LMP-1::mKate2
167 but saw no evident colocalization in intestinal cells upon *hxk-2* knockdown or control
168 conditions (**Supplementary Figure 2B-C**). We had previously shown that MML-1 localizes

169 with mitochondria in the hypodermis (Nakamura et al., 2016); however, mitochondrial
170 subcellular localization in other tissues had not been examined. Hence, we crossed the
171 MML-1::GFP strain with the mitochondrial reporter TOMM-20::mCherry under the intestinal
172 promoter *ges-1* and confirmed that MML-1 localized with mitochondria in the intestine
173 (**Figure 2D-E**). Under normal conditions, around 60-80% of the total MML-1 is nuclear, and
174 15% co-localizes with mitochondria. Interestingly, MML-1 mitochondrial localization was
175 increased to 62% of total MML-1 upon *hxk-2i* (**Figure 2F**). Taken together, our data indicate
176 that upon *hxk-2* knockdown, MML-1 is excluded from the nucleus and re-localizes to a subset
177 population of mitochondria.
178
179 *Inhibition of mitochondrial β-oxidation rescues MML-1 nuclear localization under hxk-1i*
180 Many of the genes that regulate MML-1 localization are involved in mitochondrial
181 metabolism, such as OGDC and SCS, and inhibition of these complexes could activate stress
182 response pathways. Hence, we assessed whether MML-1 nuclear localization was associated
183 with the activation of mitochondrial stress response. As a readout of mitochondrial stress, we
184 used the transcriptional reporter *hsp-6p*::GFP. As expected, we observed an increased
185 expression of *hsp-6::GFP* upon knockdown of mitochondrial components *ogdh-1*, *sucl-1*, and
186 *sucl-2* as well as in control worms treated with antimycin A (AA), a complex III inhibitor
187 (**Supplementary Figure 2D**). However, inducing mitochondrial stress with AA was not
188 sufficient to affect MML-1 nuclear localization under control conditions and *hxk-2* knockdown
189 (**Supplementary Figure 2E**). Taken together, these data indicate that MML-1 regulation by
190 glucose metabolism genes is independent of the mitochondrial stress response.
191 Hexokinase downregulation might be expected to cause a reduction in the reliance on
192 glycolysis and an increase in fatty acid metabolism as fuel for cellular maintenance (**Figure**
193 **2G**). Mitochondrial β-oxidation is an important pathway that generates acetyl-CoA for the
194 TCA cycle through the catabolism of fatty acids to produce reductants and energy. Hence, we
195 sought to investigate whether decreasing fatty acid oxidation could affect MML-1 nuclear
196 localization upon hexokinase knockdown. First, we measured the neutral lipid content by
197 feeding the worms with the labeled fatty acid C1-BODIPY-C12 and found increased total lipid
198 storage under hexokinase knockdown in the wildtype and *glp-1(e2141)* backgrounds
199 (**Supplementary Figure 2F**). Next, we measured the oxygen consumption rate (OCR) upon
200 hexokinase knockdown under basal conditions and with etomoxir supplementation, a
201 mitochondrial β-oxidation inhibitor that acts on the carnitine palmitoyltransferase (CPT).

202 Inhibition of the CPT decreases acyl-CoA import to mitochondria and changes in OCR are a
203 correlative measure of mitochondrial β-oxidation of fatty acids (Ramachandran et al., 2019).
204 We found no difference in basal OCR under *hxk-1*, *hxk-2*, and *mml-1* knockdown in the
205 wildtype background (**Figure 2H**). *glp-1(e2141)* animals showed decreased basal OCR
206 compared to wildtype, whereas *hxk-1* and *mml-1* knockdown significantly increased the basal
207 OCR compared to *glp-1(e2141)* (**Figure 2H**). Interestingly, we saw a greater percentage of
208 OCR reduction upon adding etomoxir under *hxk-1* knockdown in wildtype and under *hxk-1*,
209 *hxk-2*, and *mml-1* knockdown in *glp-1(e2141)* (**Figure 2I**), indicating higher mitochondrial
210 β-oxidation levels. We confirmed this result using the transcriptional reporter *acs-2p*::GFP,
211 mitochondrial acyl-CoA synthase, which is induced and required for fatty acid β-oxidation in
212 *C. elegans* (Van Gilst et al., 2005). We found increased *acs-2p*::GFP upon *hxk-1* and *hxk-2*
213 knockdown (**Supplementary Figure 2G**).
214 We next wondered whether this increase in fatty acid oxidation was responsible for
215 decreased MML-1 nuclear localization under hexokinase knockdown. First, we performed a
216 double knockdown of *hxk-1* or *hxk-2* combined with *acs-2*. We found that MML-1 nuclear
217 localization was rescued upon *acs-2i* under *hxk-1* knockdown (**Figure 2J**). Interestingly, *acs-2i*
218 did not rescue MML-1 nuclear localization under *hxk-2* knockdown. We also
219 pharmacologically inhibited fatty acid oxidation by supplementing etomoxir and again saw the
220 rescue of MML-1 nuclear localization under *hxk-1* knockdown but no effect upon *hxk-2*
221 knockdown (**Figure 2K**). These data suggest that HXK-1 regulates MML-1 by increasing
222 mitochondrial β-oxidation and reveal that the two hexokinases might regulate MML-1 nuclear
223 localization through somewhat independent pathways.
224
225 *hxk-2 regulates MML-1 function through increased PPP*
226 G6P can be diverted as a substrate for metabolic pathways other than glycolysis. Thus,
227 we wanted to test whether MML-1 could sense other branches of glucose metabolism. From
228 our RNAi screen, we observed increased MML-1 nuclear localization upon knockdown of two
229 enzymes from the PPP, *T25B9.9* and *tkt-1* (**Figure 1A-B**). The PPP is a cytosolic metabolic
230 pathway involved in the interconversion of 3 to 7-carbon sugars that generate precursors for
231 the biosynthesis of lipids, amino acids, and nucleotides (**Figure 3A**). It also maintains redox
232 homeostasis through NADPH production. To further address these findings, we tested the
233 effect of pharmacological inhibition PPP on MML-1 nuclear localization using
234 6-aminonicotinamide (6-AN), which is a competitive inhibitor of the G6P dehydrogenase

235 (G6DH) and phosphogluconate dehydrogenase (6PGD). These two enzymes generate NADPH
236 in the PPP. In agreement with our previous results, we observed increased MML-1 nuclear
237 localization after supplementation of 1 mM of 6-AN (**Figure 3B**). Moreover, we found that
238 *hxk-2i*, but not *hxk-1i*, significantly increased the NAPDH levels (**Figure 3C**). Additionally,
239 we found that *hxk-2i* had increased TKT-1 enzymatic activity compared to the control (**Figure**
240 **3D**), suggesting that the PPP could be enhanced in worms lacking mitochondrial hexokinase.
241 Next, we sought to test the epistatic interaction of hexokinase and PPP knockdown on
242 MML-1 nuclear localization. For these experiments, we performed double RNAi of *hxk-1* and
243 *hxk-2* in combination with the 6PGD *T25B9.9* and transketolase *tkt-1*. Interestingly, knocking
244 down these enzymes rescued MML-1 nuclear localization under *hxk-2i* (**Figure 3E-F**) but did
245 not rescue the localization under *hxk-1i* (**Supplementary Figure 3A**). To evaluate MML-1
246 function, we measured its transcriptional readouts and found that knocking down the PPP under
247 *hxk-2i* rescued the expression of *lgg-2*, *mdl-1*, *swt-1*, and *fat-5* (**Figure 3G, Supplementary**
248 **Figure 3B-D**); however, it had no effect under *hxk-1i* (**Supplementary Figure 3E-H**).
249 Moreover, we observed lower levels of G6P upon double knockdown of hexokinases with
250 *T25B9.9* and *tkt-1* compared to control (**Figure 3H, Supplementary Figure 3I**). Taken
251 together, these data suggest that the PPP activity is increased upon knockdown of the
252 mitochondrial hexokinase HXK-2, and inhibiting the PPP is sufficient to rescue MML-1
253 function independent of G6P levels.
254 Finally, we asked whether reducing the PPP could impact *glp-1(e2141)* lifespan upon
255 *hxk-2* knockdown. Inhibition of the PPP has been reported to extend the lifespan in *C. elegans*
256 by activating the mitochondrial UPR^{mt} (Bennett et al., 2017). As reported previously, we found
257 a significant lifespan extension upon *tkt-1* knockdown in wildtype (**Figure 3I**). Moreover,
258 knockdown of the PPP in the *glp-1(e2141)* background had no additive effect on longevity,
259 suggesting that *glp-1* and *tkt-1i* may share common mechanisms in extending lifespan.
260 Consistent with our data, knockdown of *T25B9.9* and *tkt-1* rescued *glp-1(e2141)* longevity
261 upon *hxk-2i* (**Figure 3I, Supplementary Figure 3J**). Collectively, these data indicate that an
262 increase in the PPP under *hxk-2* knockdown suppresses MML-1 function, and reducing PPP
263 restores longer life, placing PPP epistatically downstream of *hxk-2*.
264
265 *MML-1 interactome uncovers potential regulators of its function and localization*
266 Given the localization of MML-1 to mitochondria and possibly other organelles, we
267 decided to identify potential MML-1 binding partners to better understand its subcellular
268 distribution. We used CRISPR/Cas9 to tag the endogenous MML-1 locus with a 3xFLAG tag.

269 MML-1::3xFLAG was immunoprecipitated from whole-worm lysates and potential interactors
270 were identified by mass spectrometry. We detected ca.1600 to 2000 different proteins from
271 three biological replicates and observed that the biological replicates clustered together
272 (**Supplementary Figure 3A-B**). We detected several proteins in the immunoprecipitation (IP),
273 including MXL-2, an established MML-1 binding partner (Pickett et al., 2007), and
274 vitellogenins VIT-1, VIT-3, and VIT-4, which are highly abundant yolk proteins (**Figure 4A,**
275 **Supplementary Figure S3**). Analysis of the top 50 co-enriched candidates in MML-1 IPs
276 revealed enrichment for nuclear and mitochondrial proteins (**Supplementary Figure 4C**). We
277 also found multiple enriched proteins from different organelles, including lipid droplets (LD).
278 Mitochondria and LD dynamically interact in highly active metabolic tissues, and it has
279 been shown that mitochondria associated with LD have specific metabolic behavior compared
280 to cytosolic mitochondria (*e.g.*, different dynamics, motility, and capacity to burn
281 carbohydrates and lipids) (Gordaliza-Alaguero et al., 2019; Rambold et al., 2015). LD are
282 organelles involved in multiple roles serving as nutrient reservoirs and participating in
283 signaling pathways, and their biogenesis or degradation is tightly coupled to carbohydrate
284 metabolism (**Figure 4B**). Interestingly, PLIN-1, one of the most abundant LD proteins, was
285 co-enriched in MML-1 IP (**Figure 4A**). Hence, we wanted to test whether MML-1 localized to
286 these organelles. First, we used LipiBlue, a dye to specifically visualize LD *in vivo* (Tatenaka
287 et al., 2019), and found that all LipiBlue stained structures were positive with the LD resident
288 proteins DHS-3::GFP and PLIN-1::mCherry (**Supplementary Figure 4D-F**), indicating that
289 this dye could be used as a reliable method for visualization of LD in *C. elegans*.
290 Next, we examined LipiBlue-stained animals co-expressing MML-1::GFP and
291 TOMM-20::mCherry and saw that MML-1 localized with LipiBlue-positive structures (**Figure**
292 **4C**). Interestingly, we observed that MML-1 appeared localized to mitochondria associated
293 with LD (**Figure 4C-D**). Moreover, this colocalization was significantly increased upon *hxk-2*
294 knockdown (**Figure 4E**). Inhibition of transaldolase and enzymes from the PPP have been
295 shown to activate a fasting-like response by increasing lipolysis and enhancing the breakdown
296 of LD (Bennett et al., 2017), including higher expression of the adipose triglyceride lipase
297 ATGL-1 (**Supplementary Figure 4G**). Therefore, we wondered whether the LD size
298 correlates with MML-1 nuclear localization. We knocked down *hxk-2* and *tkt-1* to decrease and
299 increase MML-1 nuclear localization, respectively. We observed a significant reduction in
300 diameter and the total amount of LDs upon knockdown of *tkt-1*, while *hxk-2i* did not have an
301 effect (**Figure 4F, Supplementary Figure 4H).** Double knockdown of *hxk-2* and *tkt-1*,
302 however, resulted in smaller and fewer LDs than the control. Collectively, these data suggest

303 that MML-1 can localize with a specific subpopulation of mitochondria associated with LD
304 and that inhibition of the PPP can rescue MML-1 nuclear localization upon *hxk-2i* correlated
305 with decreasing LD size.

306 To test whether LDs directly regulated MML-1 localization, we knocked down *dgat-2*
307 and *atgl-1*, two enzymes involved in LD metabolism. DGAT-2 is a diacylglycerol (DAG)
308 transferase that promotes LD droplet expansion, while ATGL-1 is a rate-limiting enzyme in
309 LD breakdown (**Figure 4A**). First, we measured the neutral lipid composition and found that
310 *atgl-1i* increased lipid levels while *dgat-2i* worms did not show significant changes under *ad*
311 *libitum* conditions (**Supplementary Figure 4I**). Next, we tested MML-1 nuclear localization
312 and observed that *dgat-2i* increased MML-1 nuclear localization while *atgl-1i* resulted in
313 decreased levels of nuclear MML-1 (**Figure 4G**). Finally, we did an epistatic analysis of LD
314 metabolism and the PPP and found that MML-1 nuclear localization in *atgl-1i* was rescued
315 upon *tkt-1* knockdown (**Figure 4H**), thus, suggesting that LD metabolism is upstream or
316 parallel to the PPP in MML-1 regulation.

317

318 *The PPP regulates MondoA function in mammalian cells*

319 We next asked whether the PPP regulation of MML-1 we observed in *C. elegans* was
320 conserved in mammals. To test this, we cultured the HEK293T cells in high-glucose media
321 with 6-AN and subsequently transferred the cells to either high-glucose media or starvation
322 media (**Supplementary Figure 5A**). First, we observed decreased NAPDH/NAPD+ ratio in
323 cells treated with 6-AN and under starvation conditions (**Supplementary Figure 5B**). Next,
324 we found that in both conditions, MondoA nuclear localization was increased upon inhibition
325 of the PPP (**Figure 5A-B**), while there was no evident regulation of MondoA at the transcript
326 level (**Figure 5C**). Consistent with MondoA increased nuclear localization, we observed
327 increased expression of two of the best-described downstream targets of MondoA, *TXNIP* and
328 *ARRDC4* (**Figure 5D, Supplementary Figure 5C**). These findings indicate that the PPP also
329 regulates mammalian MondoA localization and transcriptional function.

330

331 **Discussion**

332 Nutrient sensing pathways and metabolism play a central role in modulating aging by
333 establishing metabolic states of resilience and survival. Although much work has focused on
334 identifying mediators of these processes, we still know little about how organisms coordinate
335 feedback loops of metabolic pathways and transcriptional responses to establish such states.
336 Here, we present novel mechanisms of carbohydrate and lipid metabolism regulating the

337 transcription factor MML-1/Mondo. We observed that MML-1 senses multiple steps of glucose
338 metabolism and found that hexokinases regulate MML-1 function through different
339 mechanisms in *C. elegans*. On the one hand, we found that under *hxk-2* knockdown, MML-1
340 re-localizes to mitochondria and LD, abolishing the longevity of germline-less worms and
341 mutants with reduced mitochondrial function. Moreover, we could rescue MML-1 function by
342 decreasing the PPP independent of the G6P levels. On the other hand, we found that *hxk-1*
343 knockdown decreased MML-1 function by upregulating mitochondrial β-oxidation. Thus, we
344 found two metabolic branches that converge on MML-1 to trigger a transcriptional response
345 and regulate longevity.

346 MondoA and ChREBP transcription factors have well-established central roles in
347 glucose metabolism (Ma et al., 2006; Sans et al., 2006; Stoltzman et al., 2008; Yamashita et
348 al., 2001), but whether and how glucose metabolic circuits affect Mondo regulation in a whole
349 animal model is little explored. By performing a systematic RNAi-based targeted screen of
350 enzymes involved in glucose anabolism and catabolism, we found that MML-1 senses multiple
351 steps of glucose metabolism in the worm. Among the genes tested, we found MML-1 nuclear
352 localization to be broadly sensitive to the downregulation of glycolytic enzymes, and the
353 knockdown of hexokinase had the most profound effect. Hexokinase carries out the first step
354 in glucose metabolism, the phosphorylation of glucose to form G6P, which can be shunted to
355 multiple metabolic pathways, including glycolysis, the PPP, glycogenesis, and trehalose
356 production. Our findings are consistent with previous work in cultured cells showing that
357 MondoA localization is regulated by HKII, which is thought to stimulate nuclear localization
358 via the production of G6P (Sans et al., 2006). Additionally, MondoA senses other
359 phosphorylated hexoses, including allose and 3-*O*-methylglucose (Stoltzman et al., 2011).

360 Consistent with our genetic findings above, pharmacological inhibition of glycolysis
361 by supplementation with 3-BrP and 2-DG suppressed MML-1 nuclear localization. In contrast
362 to MML-1, MondoA has been shown to accumulate in the nucleus upon 2-DG in rat L6 cells
363 (Stoltzman et al., 2008). A possible explanation for this difference is that our treatment
364 represents a chronic exposure to 2-DG from development until adulthood, while the
365 experiments in cells may reflect an acute response. Overall, 2-DG has been used as a glycolytic
366 inhibitor because it can be phosphorylated by hexokinase to 2-DG 6-phosphate; however, it
367 cannot be further metabolized in glycolysis. Further evidence shows that 2-DG not only
368 functions as a catabolic inhibitor but can also be directed to the PPP or other pathways (Chi et
369 al., 1987; Ralser et al., 2008).

370 Further, we found an important link between glycolysis and pyruvate metabolism
371 regulating MML-1 localization. Under aerobic conditions, pyruvate is imported to the
372 mitochondria and converted to acetyl-CoA to generate ATP and other reducing molecules. We
373 found that downregulation of the mitochondria pyruvate carrier *mpc-1* and the pyruvate
374 dehydrogenase complex (**Supplementary Table S1**) also decreased MML-1 nuclear
375 localization and function. Interestingly, loss of *MPC1* in yeast has been shown to accumulate
376 pyruvate, lower TCA cycle intermediates, and reduce chronological aging (Bricker et al., 2012;
377 Orlandi et al., 2014). *MPC1* similarly regulates the disposition of glycolytic and TCA
378 intermediates in flies and mammals (Bricker et al., 2012). Pyruvate can also enter the TCA
379 cycle through pyruvate carboxylase PYC-1, which converts pyruvate to oxaloacetate.
380 However, knockdown of *pyc-1* did not affect MML-1 localization (**Supplementary Table S1**),
381 suggesting that MML-1 may sense the metabolism of pyruvate mainly through oxidative
382 decarboxylation acetyl-CoA.
383 We also found that MML-1 responds strongly to alterations in the TCA cycle. The TCA
384 cycle allows organisms to oxidize carbohydrates, fatty acids, and amino acids to provide energy
385 and intermediates for the biosynthesis of macromolecules. Interestingly, the knockdown of two
386 subunits of the OGDC, *ogdh-1* and *dld-1*, increased MML-1 nuclear localization. The OGDC
387 is a rate-limiting enzyme within the mitochondrial TCA cycle that decarboxylates
388 2-oxoglutarate to succinyl-CoA. It has been shown previously that supplementation of
389 2-oxoglutarate and knockdown of *ogdh-1* extends lifespan through inhibition of ATP synthase,
390 decreasing oxygen consumption, and increasing autophagy in an mTOR-dependent manner
391 (Chin et al., 2014). Whether MML-1 is required for this lifespan extension has yet to be
392 explored. Conceivably, the mitochondrial localization of MML-1 could help sense
393 2-oxoglutarate levels, and the accumulation of this metabolite could signal translocation to the
394 nucleus. Moreover, glutamine can be converted to glutamate and subsequently to
395 2-oxoglutarate during glutaminolysis and represents an important mechanism to replenish the
396 TCA cycle under different metabolic challenges. In this case, OGDC plays a pivotal role in
397 channeling anaplerotic reactions into the TCA cycle from glutamine and glutamate and other
398 amino acids that can ultimately be converted to 2-oxoglutarate (*i.e.*, histidine, proline, and
399 arginine) (Owen et al., 2002). Interestingly, increased glutamine-dependent anaplerosis has
400 been shown to regulate MondoA activity in BxPC-3 cells (Kaadige et al., 2009), though the
401 molecular mechanism remains unclear. Whether glutamine, glutamate supplementation, or
402 knockdown of glutamate dehydrogenase can regulate MML-1 nuclear localization remains to
403 be determined.

404 On the other hand, the TCA cycle can operate in reverse to restore TCA intermediate
405 levels (Dalziel & Londesborough, 1968). Increased levels of 2-oxoglutarate due to inhibition
406 of OGDC, or glutamine anaplerosis, can undergo reductive carboxylation by isocitrate
407 dehydrogenase to produce isocitrate. After that, aconitase can convert isocitrate to citrate,
408 which can be exported out of the mitochondria for *de novo* lipogenesis. MML-1 could help
409 orchestrate the metabolic rewiring of the TCA cycle with the fatty acid metabolism
410 transcriptional response. Notably, ChREBP has been shown to regulate many lipogenic
411 enzymes, including acetyl-CoA carboxylase (ACC), the fatty acid synthase (FAS), and
412 ATP-citrate lyase (ACLY) (Ishii et al., 2004; Postic et al., 2007). Accordingly, the MML-1
413 transcriptome shows clear regulation of several fatty acid metabolic enzymes (Nakamura et al.,
414 2016).
415 We observed that PPP pathway enzymes also strongly influenced MML-1 nuclear
416 localization and function. The PPP is a cytosolic pathway involved in the interconversion of
417 sugars to generate precursors for the biosynthesis of lipids, amino acids, and nucleotides and
418 maintain redox homeostasis. We found that knockdown of PPP components, PGDH *T25B9.9*
419 and transketolase *tkt-1*, enhanced MML-1 nuclear localization, increased the transcription of
420 MML-1 target genes, and restored longevity to *glp-1(e2141)* animals under *hxk-2i*. The PPP is
421 the primary source of NADPH, which plays a vital role in many cellular processes, including
422 fatty acid, nucleotide, neurotransmitter, and cholesterol metabolism, and works as an essential
423 reducing agent (Ju et al., 2020). We found that pharmacological inhibition with 6-AN of the
424 two enzymes producing NADPH in the PPP increased MML-1 nuclear localization. We also
425 found increased levels of NADPH and lower levels of G6P under *hxk-2* knockdown.
426 Importantly, these observations suggest that residual G6P may be diverted to the PPP under
427 low mitochondrial hexokinase and further imply that metabolites other than G6P could regulate
428 MML-1 nuclear localization. What this other metabolite could be remains elusive, but a
429 simplifying notion is that MML-1 nuclear localization is promoted by intermediates in the
430 glycolysis or the PPP. Blocking entry into the PPP or TCA might be expected to accumulate
431 such metabolites and promote Mondo nuclear localization. Conversely, depletion of these
432 metabolites would disrupt Mondo nuclear localization and activity.
433 Another possibility is that Mondo organellar distribution is regulated at another scale.
434 Notably, a major output of the PPP and NADPH metabolism is the production of lipids.
435 Interestingly, we found that under *tkt-1* knockdown, fat levels decreased, and LDs were smaller
436 in diameter, suggesting that a reduction in LDs could signal MML-1 to translocate to the
437 nucleus. Consistently, transaldolase *tald-1* knockdown has been shown to increase lifespan and

438 decrease intestinal fat levels in the worm through increased activity of adipose triglyceride
439 lipase ATGL-1 (Bennett et al., 2017). This enzyme is involved in the metabolism of LD under
440 starvation to mobilize stored fats for energy production (Lee et al., 2014).

441 Interestingly, we found that although both HXK-1 and HXK-2 positively regulate
442 MML-1 function, they do so through different mechanisms. We observed that inhibiting
443 mitochondrial fatty acid β-oxidation is sufficient to rescue MML-1 nuclear localization under
444 *hxk-1* knockdown, but not *hxk-2* knockdown. Conversely, decreasing the PPP rescued MML-1
445 localization under *hxk-2* knockdown independent of the G6P levels, but not *hxk-1* knockdown.
446 How both hexokinases activate different metabolic pathways to regulate MML-1 remains
447 unknown and could work at multiple levels.

448 First, there is evidence that differences in the subcellular location of hexokinases may
449 result in the compartmentalization of glucose metabolism, with channeling of G6P to different
450 pathways (John et al., 2011; Wilson, 2003). Mitochondrial hexokinase has preferential access
451 to ATP generated in the mitochondria and provides efficient glycolysis coupling with further
452 pyruvate oxidation by the TCA cycle and oxidative phosphorylation (OXPHOS). Furthermore,
453 mammalian HKI and HKII have a dynamic localization, shuttling between the mitochondrial
454 outer membrane and the cytoplasm (John et al., 2011). Both mammalian hexokinases have
455 been reported to reversibly bind to mitochondria through their N-terminal sequence (Roberts
456 et al., 2014) and via their interaction with VDAC1 (Lindén et al., 1982). This dual localization
457 allows the cell to adapt to different metabolic requirements and maintain energetic balance.
458 Under high levels of G6P, HKII shuttles from the mitochondria to the cytoplasm, causing cells
459 to use glycogen as an energy source (John et al., 2011). The subcellular localization also plays
460 other significant roles in different signaling pathways. For example, mitochondria-bound
461 hexokinase has anti-apoptotic effects (Gottlob et al., 2001), and increased N-acetylglucosamine
462 upon pathogen exposure releases hexokinase from the mitochondria and activates innate
463 immune responses (Wolf et al., 2016). Here we found that *C. elegans* HXK-2 is associated with
464 mitochondria and that this localization is abolished by the deletion of the first ten amino acids.
465 However, we saw no effect upon *vdac-1* knockdown nor dynamic localization of HXK-2
466 between mitochondria and cytosol (data not shown). Taken together, these observations
467 suggest that the nematode has dedicated mitochondrial (HXK-2) and cytosolic (HXK-1 and
468 HXK-3) hexokinases.

469 We also found differences in the tissue expression of the different hexokinase isozymes
470 of the nematode: HXK-1 was mainly found in the pharynx, neurons, gonadal sheath, and

471 coelomocytes, while HXK-2 was present in the hypodermis, body wall muscle, and intestine.
472 Consistently, RNAseq data from different tissues in *C. elegans* shows that *hxk-2* is the main
473 isozyme in the body wall muscle and intestine (Hutter & Suh, 2016). At the same time, *hxk-1*
474 is the main one expressed in pharyngeal muscle and neurons. This differential distribution
475 could explain how *hxk-1* and *hxk-2* differentially regulate MML-1 through β-oxidation and
476 PPP pathways. Notably, we scored MML-1 nuclear localization in the intestine for most
477 experiments, where *hxk-2* but not *hxk-1* is expressed. In the future, it will be important to see
478 whether *hxk-1* cell autonomously impacts *mml-1* nuclear localization within the same tissue,
479 such as the pharynx.

480 In any case, our observation that HXK-1 affects intestinal MML-1 nuclear localization
481 suggests cell non-autonomous signaling. What might be the nature of such cell non-
482 autonomous signaling? One possibility is the sterol hormone signaling pathway, which acts in
483 somatic reproductive tissue to regulate *glp-1(e2141)* longevity. Decreasing the activity of the
484 nuclear hormone receptor DAF-12, or its ligands dafachronic acids, abolishes the longevity of
485 germline-less worms (Gerisch et al., 2001; Yamawaki et al., 2010). Interestingly, carbohydrate
486 metabolism directly impacts the production of dafachronic acids as NADPH is required for the
487 last step of dafachronic acid biosynthesis by DAF-9 (Motola et al., 2006; Penkov et al., 2015).
488 Furthermore, DAF-9 is expressed in the somatic gonad (spermatheca) and XXX neurons in
489 adult animals (Gerisch & Antebi, 2004). Conceivably, downregulation of hexokinase could
490 affect the production of NADPH and dafachronic acids regulating DAF-12 activity, thereby
491 affecting MML-1 function. It will be interesting to see whether dafachronic acid
492 supplementation can rescue MML-1 nuclear localization upon *hxk-1i* or *hxk-2i*.

493 The nervous system also plays a crucial role in integrating metabolic status and
494 systemic responses in a cell non-autonomous manner (Mutlu et al., 2020; Zhang et al., 2019).
495 Inhibition of the mTOR signaling pathway has been shown to extend lifespan across the
496 evolutionary spectrum (Kennedy & Lamming, 2016), and recent work has shown that restoring
497 *raga-1/*RagA or *rsks-1/*S6K in the nervous system is enough to entirely suppress the lifespan
498 extension conferred by mutation of these mTOR signaling factors (Zhang et al., 2019). In cells,
499 HKII has been shown to shuttle from the mitochondria and directly interact with mTOR under
500 glucose deprivation and inhibit its function resulting in an induction of autophagy (Roberts et
501 al., 2014). This interaction is dependent on the mTOR signaling (TOS) motif present in HKII
502 required for binding to Raptor. Interestingly, this TOS motif (KDIDI) is conserved in the
503 nematode HXK-1; however, HXK-2 and HXK-3 lack this sequence. It would be interesting to

504 study whether the interaction between hexokinase and mTOR is conserved in *C. elegans* and
505 whether decreasing the main neuronal hexokinase (HXK-1) would result in mTOR-dependent
506 inhibition of MML-1.

507 Proteins tend to co-localize near their substrates to maximize specificity and regulate
508 signaling pathways. In particular, MondoA was first reported to be associated with the
509 mitochondria outer membrane in primary human SkMC cells through protein-protein
510 interaction (Sans et al., 2006). We have previously shown that this localization is conserved in
511 *C. elegans* (Nakamura et al., 2016). Mitochondria-bound MondoA has been proposed to have
512 preferential access to newly synthesized G6P from HKII to coordinate metabolism and
513 transcriptional response (Wilde et al., 2019). However, the identity of the mitochondrial factor
514 tethering MondoA at the mitochondria remains unknown.

515 Interestingly, our proteomics analysis of MML-1 immunoprecipitation showed
516 enrichment with proteins from different cellular compartments, including mitochondria, ER,
517 LD, and nucleolus, suggesting an important role of Mondo in integrating diverse organellar
518 signals. Localization to mitochondria was particularly conspicuous. Multiple nuclear
519 transcription factors are localized in the mitochondria, although dissecting their nuclear and
520 mitochondrial function is challenging (Leigh-Brown et al., 2010). On the one hand, nuclear
521 transcription factors have been shown to directly bind the mitochondrial genome to regulate
522 transcription, such as the cAMP response element-binding (CREB) protein (Marinov et al.,
523 2014). Interestingly, *mml-1(ok849)* loss-of-function mutants showed a decrease in all 12
524 mitochondrial-encoded genes compared to wildtype (Nakamura et al., 2016). However, this
525 could be indirect by regulating the mitochondrial transcription factor TFAM or mitochondrial
526 biogenesis (Li et al., 2005). On the other hand, transcription factors like p53 have been shown
527 to translocate to the mitochondrial outer membrane under apoptotic signals to interact with
528 Bcl-2 and promote membrane permeabilization and apoptosis (Marchenko et al., 2007). Future
529 studies will help elucidate whether MML-1/MondoA mitochondrial localization regulates
530 other cellular processes independent of its nuclear transcription function.

531 LD represents the main lipid storage in cells to balance metabolism and energy
532 demands. These organelles are essential for many signaling pathways and are required for
533 survival during fasting by mobilizing lipids for energy production. In *C. elegans,* LDs are
534 mainly localized in the intestine and hypodermis and are composed almost exclusively of TAG
535 (Vrablik et al., 2015). We found PLIN-1, one of the most abundant LD proteins, enriched in
536 the MML-1 interactome. Interestingly, we found that MML-1 colocalizes with LD *in vivo* in
537 the intestine. MondoA was previously seen in large-scale proteomics associated with LD

538 (Krahmer et al., 2018). It was shown that MondoA and Mlx localized with LD through
539 amphipathic helices in the C-terminus in SUM159 cells (Mejhert et al., 2020). The researchers
540 proposed a model in which MondoA/Mlx colocalization with LD inhibits its transcriptional
541 activity limiting glucose-dependent transcription. More recently, work by Brunet and
542 colleagues suggest that MUFA intercalation into LD and peroxisomes promote longevity,
543 though downstream transcription factors are little explored (Papsdorf et al., 2023).
544 Mitochondria and LD physically interact with one another to regulate metabolism (Boutant et
545 al., 2017). As MondoA has also been shown to localize with mitochondria, it would be
546 interesting to understand the role of this organelle in regulating MondoA association with LD.
547 Although the proteins involved in these contact sites are just beginning to be uncovered, both
548 PLIN1/PLIN-1 and ACSL1/ACS-13 have been proposed to tether mitochondria and LD
549 (Gordaliza-Alaguero et al., 2019).
550 Mitochondria bound to LD facilitate the coordination of TAG metabolism and fatty
551 acid oxidation. For example, lipases (*e.g.*, ATGL) in the LDs break down TAG to release free
552 fatty acids that can be activated in the mitochondria outer membrane by ACSL1 to fatty
553 acyl-CoA. This acyl-CoA can be imported into the mitochondria for β-oxidation. We propose
554 a model in which MML-1 interacts with specific mitochondria associated with LD to
555 orchestrate a transcriptional response depending on fuel utilization. Under normal conditions,
556 glucose stimulates MML-1 translocation to the nucleus to activate the transcription of
557 glycolytic enzymes. In contrast, upon blockage of glycolysis (*e.g.,* hexokinase knockdown),
558 the cell utilizes fatty acids to produce ATP, re-localizing and inhibiting MML-1 at the
559 mitochondria-associated with LD.
560
561 **Materials and Methods**
562 *Worm growth and RNAi treatment*
563 *C. elegans* worm strains were grown and maintained on nematode growth medium
564 (NGM) plates seeded with *E. coli* OP50 strain as the primary food source. Worms were grown
565 at 20 °C unless stated otherwise. *glp-1(e2141)* strains were maintained at 15 °C. All worm
566 strains are listed in **Supplementary Table S4**. Worms were synchronized by 4 to 6 h egg lays
567 at 20 °C. For experiments including *glp-1(e2141)*, egg lays were performed at 15 °C, and the
568 eggs were upshifted to 25 °C for 52 to 56 h to induce the germline-less phenotype. After *glp-1*
569 induction, worms were downshifted to 20 °C until the day of analysis or collection.

570 The NGM media for RNAi knockdown was supplemented with 1 mM isopropyl
571 β-1-D-thiogalactopyranoside (IPTG) and 100 μg mL^{-1} ampicillin. The plates were seeded with
572 the RNAi-expressing *E. coli* HT115 (DE3) strain transformed with the L4440 vector from the
573 Ahringer and Vidal libraries (Kamath & Ahringer, 2003; Rual et al., 2004), or cloned for this
574 work. Bacteria containing luciferase RNAi cloned into the L4440 vector were used as controls.
575 Worms were grown on RNAi plates egg-on in all the experiments.
576
577 *Cell culture experiments*
578 HEK293T cells were maintained in DMEM medium 4.5 g/L D-glucose (Gibco)
579 supplemented with 10% FBS (Gibco). For blocking the PPP, cells were supplemented with 16
580 and 100 μM 6-AN for 24 to 48 h. After, cells were washed and added fresh DMEM medium
581 or transferred to starvation media (NaCl 140 mM, $CaCl_2$ 1 mM, $MgCl_2$ 1 mM, HEPES pH 7.4
582 20 mM, BSA 1%) for 6 h. Cells were collected for immunofluorescence, RNA extraction, and
583 metabolite quantification.
584 For addressing MondoA localization, cells were fixed with 4% paraformaldehyde (PFA) for
585 15 min at room temperature. Following fixation, the samples were washed 3 times with 500
586 μL DPBS, followed by 500 μL of methanol 99% for 5 min at -20 °C, and washed twice with
587 500 μL of DPBS and three times with TBST 1X. Cells were blocked with 10% goat serum
588 diluted in DPBS for 1 h at room temperature. Cells were incubated with 200 μL of the Anti-
589 MondoA antibody (Bethyl Laboratories, A303-195A) 1:500 diluted in goat serum overnight at
590 4 °C. Next, cells were washed 3 times with DPBS containing Triton x-100 (PBST) and similarly
591 incubated with 200 μL of Alexa-488 secondary antibody (Invitrogen, A21206) 1:500 diluted
592 in the goat serum at room temperature and covered in aluminum foil for 2 h. After washing 3
593 times with 500 μL of PBST, the samples were covered with a mounting medium containing
594 DAPI. The cells were cured for 24 h at room temperature in the dark and then stored at 4 °C.
595
596 *Demographic analysis*
597 Lifespan analyses were conducted by synchronizing worms by egg lay. All animals
598 were kept at 20 °C egg on, or transferred to 20 °C on day one of adulthood for the experiments
599 including *glp-1(e2141)*. More than 120 worms were used per strain/condition with 20-30
600 worms per 6 cm plate. Worms were transferred every other day to fresh plates until they
601 stopped laying eggs and scored every time they were transferred. Animals with internal
602 hatching and vulva protrusions were censored from the analysis. All lifespans were performed

603 by blinding the genotypes/RNAi. Demographic parameters like mean, median, and maximum
604 lifespan were calculated and plotted using GraphPad Prism 9 software.
605
606 *Oxygen consumption rate measurements*
607 Oxygen consumption rates (OCR) measurements in *C. elegans* were based on
608 (Koopman et al., 2016). Worms were synchronized by egg lay. 10 to 15 adult worms were
609 transferred to a Seahorse XF96 Cell Culture Microplate (Agilent) with 200 μL of M9 buffer.
610 OCR was measured using the Seahorse XFe96 Analyzer (Agilent). To measure mitochondrial
611 fatty acid β-oxidation, basal oxygen consumption was measured followed by injection of
612 etomoxir (final well concentration 500 μM) and finally injection of sodium azide (final well
613 concentration 40 mM), all measured five times. OCR was normalized to the number of worms
614 with at least six technical replicates.
615
616 *Body measurements, pharyngeal pumping rates, and motility assay*
617 Worms were imaged or recorded using the Leica stereo microscope MDG41 equipped
618 with Leica DFC3000G monochrome camera with a 6.3X magnification. For measuring the
619 body length and area, >20 worms were transferred to a drop of sodium azide 50 mM, imaged,
620 and analyzed in Fiji imaging software. To measure the pharyngeal pumping rates, worms were
621 transferred to a new plate, acclimated on the plates without a lid for 10 min, and then recorded
622 for 30 s. Worm motility was assessed by placing >20 worms in a drop of M9 buffer and
623 recorded for 30 s using the Leica M80 Binocular Microscope equipped with the Leica MC170
624 HD camera. Videos were analyzed to count the thrashing of each worm.
625
626 *Molecular cloning*
627 Plasmids were constructed by classical cloning or Gibson Assembly. Restriction
628 enzymes from NEB were used according to the manufacturer's instructions. Custom primers
629 were designed with SnapGene v.5.3.2 and NEBuilder Assembly Tool v.2.5.4 (**Supplementary**
630 **Table S5**). For classical cloning, digested plasmids and amplicons were ligated using the T4
631 DNA Ligase according to the manufacturer's instructions (New England Biolabs). For Gibson
632 Assembly, digested plasmid and amplicon were assembled using NEBuilder HiFi DNA
633 Assembly Master Mix (New England Biolabs) according to the manufacturer's instructions.
634 Plasmids were transformed into *E. coli* DH5α (Life Technologies) strain using the heat shock
635 protocol and plated on LB media supplemented with ampicillin.

636

637 *RNA extraction and RT-qPCR*

638 Worms were synchronized by egg lay for 4 h and collected once they reached the young
639 adult stage in 15 mL conical tubes. The worm pellet was subjected to 4 cycles of freeze and
640 thaw with liquid nitrogen and a water bath at ~37 °C. To lyse the worms, 200 µL of 1.0 mm
641 Zirconia/Silica beads (FisherScientific) were added and transferred to the TissueLyser LT
642 (Qiagen) for 30 min, full speed at 4 °C. Samples were incubated for 5 min at RT. After, 200
643 µL chloroform was added and centrifuged at 12,000 g for 15 min at 4 °C. The top aqueous
644 phase was transferred to a new 1.5 mL tube and mixed with 200 µL of ethanol. The RNA
645 purification was performed using the RNeasy Mini Kit (Qiagen) according to the
646 manufacturer's instructions. The concentration and purity of the RNA samples were quantified
647 using the NanoPhotometer NP80 spectrophotometer (Implen).

648 cDNA was prepared after extracting total RNA from young adult worms or cell extracts
649 using the iScript cDNA Synthesis Kit (BioRad) according to the manufacturer's instructions.
650 Primers, cDNA, and Power SYBR Green Master Mix (Applied Biosystems) were transferred
651 to a 384-well plate using the JANUS automated workstation (PerkinElmer) with four technical
652 replicates per genotype/gene. The reaction was quantified using the ViiA 7 Real-Time PCR
653 system machine (Applied Biosystems). *cdc-42* was used as an endogenous control for the
654 quantification. The complete primer sequences are in **Supplementary Table S5**.

655

656 *Protein extraction and Western blot analysis*

657 Worms were harvested from a mixed population or synchronized by egg lay or
658 bleaching with M9 buffer and washed three times. The worm pellet was snap-frozen in liquid
659 nitrogen and stored at -80 °C until extraction. The pellet was resuspended in liquid lysis buffer
660 supplemented with cOmplete ULTRA EDTA-free protease inhibitors (Roche) and PhosSTOP
661 phosphatase inhibitors (Roche) and sonicated with Bioruptor Plus (Diagenode S.A.) coupled
662 to Minichiller 300 (Huber) for 15 cycles of 30 sec sonication, 30 sec rest at 4 °C. The total
663 protein extract was cleared by spinning down at 20,817 g for 10 min at 4 °C. Supernatant was
664 transferred to a new tube, and protein was quantified using Pierce BCA Protein Assay Kit
665 (ThermoFisher Scientific) according to the manufacturer's instructions. Equal amounts of
666 protein were mixed with 4X loading sample buffer containing DTT 50 mM and boiled at 95
667 °C for 10 min. Samples were loaded onto an SDS-PAGE PERCENTAGE gel (BioRad), and
668 proteins were then transferred onto a nitrocellulose membrane (BioRad) using the Trans-Blot

669 Turbo Transfer System (BioRad). Membranes were blocked for 1 h at RT with 5% milk in
670 TBST. Primary and secondary antibodies were diluted in 5% bovine serum albumin (BSA) in
671 TBST and incubated for 2-18 h at 4 °C. Antibodies: RFP Tag Polyclonal Antibody 1:1000
672 (ThermoFisher Scientific, R10367), Monoclonal ANTI-FLAG M2, Clone M2 1:1000 (Sigma
673 Aldrich, F1804), Anti-beta Actin Antibody 1:1000 (Abcam, Ab8224), Anti-rabbit IgG (H+L)
674 1:5000 (Invitrogen, G21234), Anti-mouse IgG 1:5000 (Invitrogen, G21040), Rabbit Anti-
675 Mouse IgG (Ligh Chain Specific) (D3V2A) mAB (HRP Conjugate) 1:5000 (CST, 58802). The
676 membranes were washed three times with TBST for 10 min at RT in-between incubation with
677 the antibodies and after the secondary. The signals were detected using Western Lightning
678 Plus-ECL, Enhanced Chemiluminescence Substrate (PerkinElmer), and imaged in the
679 ChemiDoc MP Imaging System with Image Lab software (BioRad).
680
681 *Immunoprecipitation*
682 Worms were collected from a mixed population from twenty 10 cm plates, transferred
683 into 15 mL conical tubes with M9 buffer, and washed three times. Worms were snap-frozen in
684 liquid nitrogen and stored at -80 °C until extraction. The worm pellet was resuspended in lysis
685 buffer supplemented with cOmplete ULTRA EDTA-free protease inhibitors (Roche) and
686 PhosSTOP phosphatase inhibitors (Roche). Worms were sonicated with Bioruptor Plus
687 (Diagenode S.A.) coupled to Minichiller 300 (Huber) for 30 cycles of 30 sec sonication, 30 sec
688 rest at 4 °C. The total extract was cleared by spinning down at 20,817 g for 15 min at 4 °C.
689 Supernatant was transferred to a new tube, and protein was quantified using Pierce BCA
690 Protein Assay Kit (ThermoFisher Scientific) according to the manufacturer's instructions.
691 The Anti-FLAG M2 magnetic beads (Sigma) were resuspended and equilibrated with
692 TBST buffer. A total of 7 mg of total protein extract in 800 µL was mixed with the magnetic
693 beads and incubated overnight at 4 °C. The next day, the supernatant was removed and stored
694 for WB analysis. The beads were washed 3 times with 1 mL of cold washing buffer #1
695 (Tris/HCl, pH 7.4 20 mM, NaCl 300 mM, EDTA 1 mM, NP-50 0.5%), and 3 times with 1 mL
696 of cold washing buffer #2 (Tris/HCl, pH 7.4 20 mM, NaCl 300 mM, EDTA 1 mM). In the last
697 wash, 500 µL of washing buffer #2 was added, and 100 µL were stored for WB analysis.
698 To elute samples for mass spectrometry, 100 µL of elution buffer (Trypsin 5 ng/µL,
699 Tris/HCl, pH 7.5 50 mM, Tris(2-carboxyethyl)phosphine (TCEP) 1 mM, Chloroacetamide
700 (CAA) 5 mM) were added and incubated 30 min at RT. The supernatant was transferred to a

701 new 0.5 mL tube and incubated overnight at 37 °C. The next day, formic acid was added to a
702 final concentration of 1% to stop the digestion. Peptides were stored at -20 °C until purification.
703 The peptides were cleaned and purified with StageTip. A 30 µg C18-SD tip was
704 hydrated with 200 µL of methanol, followed by 200 µL of 40% acetonitrile (ACN)/0.1% formic
705 acid (FA). 200 µL of 0.1% FA were added to equilibrate the C18-SD. The digested peptides
706 were dissolved in 0.1% FA and added to the C18-SD and washed once with 0.1% FA. To elute
707 the peptides, 80 µL of 40% ACN/0.1% FA was added, and elutes were collected in 0.5 µL
708 tubes and dried in centrifugal vacuum Concentrator Plus (Eppendorf) for 45 min at 45 °C.
709
710 *LC-MS/MS analysis*
711 Peptides were separated on a 25 cm, 75 µm internal diameter PicoFrit analytical column
712 (New Objective) packed with 1.9 µm ReproSil-Pur 120 C18-AQ media (Dr. Maisch) using an
713 EASY-nLC 1200 (ThermoFisher Scientific). The column was maintained at 50 °C. Buffer A
714 and B were 0.1% FA in water and 0.1% FA in 80% CAN, respectively. Peptides were separated
715 on a segmented gradient from 6 to 31% buffer B for 57 min and from 31 to 44% buffer B for
716 5 min at 250 nl/min. Eluting peptides were analyzed on an Orbitrap Fusion Tribrid mass
717 spectrometer (ThermoFisher Scientific). Peptide precursor m/z measurements were carried out
718 at 60,000 resolution in the 350 to 1,500 m/z range. The most intense precursors with charge
719 states from 2 to 7 were selected for HCD fragmentation using 27% normalized collision energy.
720 The cycle time was set to 1 sec. The m/z values of the peptide fragments were measured at a
721 resolution of 50,000 using an AGC target of 2e5 and 86 ms maximum injection time. Upon
722 fragmentation, precursors were put on a dynamic exclusion list for 45 sec.
723 The raw data were analyzed with MaxQuant v.1.6.1.0 (Cox & Mann, 2008). Peptide
724 fragmentation spectra were searched against the canonical and isoform sequences of the *C.*
725 *elegans* reference proteome (proteome ID UP000001940, downloaded December 2018 from
726 UniProt). Methionine oxidation and protein N-terminal acetylation were set as variable
727 modifications; cysteine carbamidomethylation was set as fixed modification. The digestion
728 parameters were set to "specific" and "Trypsin/P". The minimum number of peptides and razor
729 peptides for protein identification was 1; the minimum number of unique peptides was 0.
730 Protein identification was performed at a peptide spectrum match and protein false discovery
731 rate of 0.01. The "second peptide" option was on. Successful identification was transferred
732 between the different raw files using the "Match between runs" option. Label-free
733 quantification (LFQ) (Cox et al., 2014) was performed using an LFQ minimum ratio count of

734 2. LFQ intensities were filtered for at least two valid values in at least one group and imputed
735 from a normal distribution with a width of 0.3 and a downshift of 1.8. Differential expression
736 analysis was performed using *limma* package v.3.34.9 (Ritchie et al., 2015) in R v.3.4.3 (R
737 Core Team, 2017).
738
739 *G6P and $NADP^+$/NADPH measurements and TKT activity assay*
740 G6P and $NADP^+$/NAPDH were measured from total worm extracts or cell extracts
741 using the Glucose-6-Phosphate Assay Kit (Sigma MAK014) and the NADP/NADPH-Glo
742 Assay (Promega G9081), respectively, following the manufacturer's instructions. The
743 Transketolase Activity Assay Kit (Fluorometric) (Sigma MAK420) was used to measure TKT
744 activity in worm extracts following the manufacturer's instructions. Samples were normalized
745 to total protein concentration.
746 *glp-1(e2141)* strains were used to avoid signals from the germline. Briefly, worms were
747 synchronized as mentioned previously, collected in a 15 mL conical tube, and washed three
748 times with M9 buffer. Worms were snap-frozen in liquid nitrogen and sonicated using the
749 Bioruptor Plus (Diagenode S.A.) coupled to Minichiller 300 (Huber) for 15 cycles of 30 sec
750 sonication, 30 sec rest at 4 °C. Worms' extracts were cleared by centrifugation at 20,817 g for
751 15 min at 4 °C. Samples were always kept on ice. As mentioned previously, part of the samples
752 was used to quantify protein, and the rest was used to quantify the metabolites.
753 For G6P colorimetric detection, samples were run in technical duplicates in a 96-well
754 plate. The standard curve was made using the G6P Standard solution provided by diluting with
755 ddH_2O to generate 0 (blank), 2, 4, 6, 8, and 10 nmol/well standards. Samples were combined
756 with the reaction mix in each well and mixed for 30 min at RT, protecting the plate from the
757 light. The absorbance was measured at 450 nm using the POLARstar OMEGA Plate Reader
758 with Luminescence (BGM Labtech). For the analysis, all samples were corrected for the
759 background. The standard curve was generated with the appropriate values obtained by the
760 standards mentioned previously, and the amount of G6P in each sample was calculated with
761 the standard curve. Values were normalized to protein levels.
762 For the $NADP^+$/NADPH bioluminescent assay, samples were run in technical
763 duplicates in a 96-well plate. 50 µL of worm lysis in M9 buffer were incubated with 50 µL
764 base solution with 1% DTAB. Samples were split into two: one to measure $NADP^+$ and the
765 other to measure NADPH. Samples were incubated with or without 25 µL 0.4 N of HCl to
766 measure $NADP^+$ or NADPH, respectively, at 60 °C for 15 min, and then the plate was

767 equilibrated for 10 min at RT. Next, 25 µL of Trizma base were added to each well of acid-
768 treated samples to neutralize the acid and 50 µL of HCl/Trizma solution to each well of base-
769 treated samples. An equal amount of the NADP/NADPH-Glo Detection Reagent was added to
770 each well and mixed at RT for 30 min by protecting the plate from the light. The luminescence
771 was recorded using the POLARstar OMEGA Plate Reader with Luminescence (BGM
772 Labtech). Samples were corrected to background luminescence. The relative luminescent units
773 were standardized to the protein concentration.
774
775 *Brightfield and fluorescent imaging*
776 Brightfield and fluorescent images with higher resolution were acquired using the Zeiss
777 Axio Imager Z1 Fluorescent Microscope equipped with the Digital Microscope Camera Axio
778 Cam Mono 506 and the IcC5 true color camera. For fluorescent microscopy, the microscope
779 used a Colibri 7 LED Light Source and the filters sets GFP (Set 38 HE), TR (Set 45), and TL.
780 The software used was Zeiss Zen v2.3.69.1017. Brightfield and fluorescent images were also
781 acquired with the Leica stereo microscope MDG41 equipped with Leica DFC3000G
782 monochrome camera. The microscope was equipped with the Leica EL6000 external light
783 source. The software used was the Leica Application Suite X v3.7.5.24914.
784 All dyes were added to the bacterial lawn, incubated egg on, and protected from the
785 light until the day of imaging. Final solutions were made by diluting in M9 buffer. LipiBlue
786 (Dojindo) was resuspended in 100 µL of DMSO to make a 100 µM stock. The final
787 concentration used was 1 µM. C1-BODIPY-C12 500/510 (ThermoFisher Scientific) was
788 dissolved in DMSO to make a 5 mM stock. The final concentration used was 1 µM. Worms
789 were mounted on a slide with a 5% agarose pad using sodium azide 50 mM. Levamisole 2 mM
790 was used as an anesthetic to image mitochondria.
791 Nuclear localization of MML-1::GFP was quantified in intestinal cells from day one
792 adult worms. Worms anesthetized with sodium azide 40 mM. At least, 20 worms were imaged
793 per genotype/condition. Quantification of the transcription factor nuclear localization was
794 performed by manually selecting each nucleus and calculating the pixel intensity per area. The
795 same area was used to calculate the cytosolic and background signal. Values were corrected by
796 background subtraction. Nuclear localization was calculated by dividing the nuclear signal
797 from the cytosolic signal.
798
799 *Confocal Imaging*

Confocal images were acquired with Leica TCS SP8 confocal microscope equipped with a white light laser and a 63X 1.4 NA oil objective. The microscope was also equipped with HyD detectors for fluorescent images and a PMT detector for the bright field. The LAS X Life Science software was used to acquire images and 3D reconstruction. When multiple fluorescent proteins or dyes were imaged, sequential scanning was used to reduce the bleed-through of the signal from one channel to another. All images used for colocalization analysis were deconvoluted with the installed LIGHTNING package to optimize the images and reduce background noise.

Statistical analysis and software

The results are presented as mean + SD or SEM, as the figure legends indicate. The number of biological replicates is shown in the figure legends as "N", while the number of worms is presented as "n". Before comparing groups, the data were tested for Gaussian distribution using the Kolmogorov-Smirnov normality test with Dallal-Wilkinson-Lilliefor *p*-value. For normally distributed data, unpaired *t*-test with Welch's correction or one-way ANOVA with Brown-Forsythe and Welch's corrections were calculated in GraphPad Prism 9 (GraphPad software). For lifespan analysis, *p*-values were calculated using Log-rank (Mantel-Cox) test. Statistical data from all the lifespans are included in **Supplementary Table S2**. Statistical significance for qPCR experiments was calculated with two-tailed *t*-test. For colocalization analysis, Costes' randomization was performed to determine statistical significance. Significance levels are ns = not significant $p>0.05$, * $p<0.05$, ** $p<0.01$, *** $p<0.001$, **** $p<0.0001$.

Image analysis was performed using open-source Fiji package software. Additional JACoP (Bolte & Cordelières, 2006) plugin was used for colocalization analysis. Densitometry analyses were performed using GelAnalyzer v.19.1. Graphs were generated in GraphPad Prism 9 and using custom R scripts.

Acknowledgments

We would like to thank the CGC (University of Minnesota) and SunyBiotech for some of the strains used in this study. We also thank Katrin Wollenweber, Tim Droth, and Nadine Hochhard for their technical assistance and the Proteomics, Bioinformatics, and FACS & Imaging Core Facilities at the MPI AGE for their support. Special thanks to Özlem Karalay, Andrea Annibal, Roberto Ripa, Sarah Kreuz, and Victoria Martínez Miguel for the discussions

and comments. This work was funded by the Max Planck Society and the Cologne Graduate School for Ageing Research (CGA).

Authors contributions

A.A. and R.L. designed the experiments and wrote the manuscript. R.L. performed most of the experiments. M.N. established and performed the MondoA localization upon PPP inhibition in cell culture, M.V. acquired and processed the samples for proteomics and repeated biological replicates, E.B. measured the NADPH/$NADP^+$ levels in mammalian cells, I.A. performed proteomics.

Competing interests

The authors declare no competing interests.

Figures

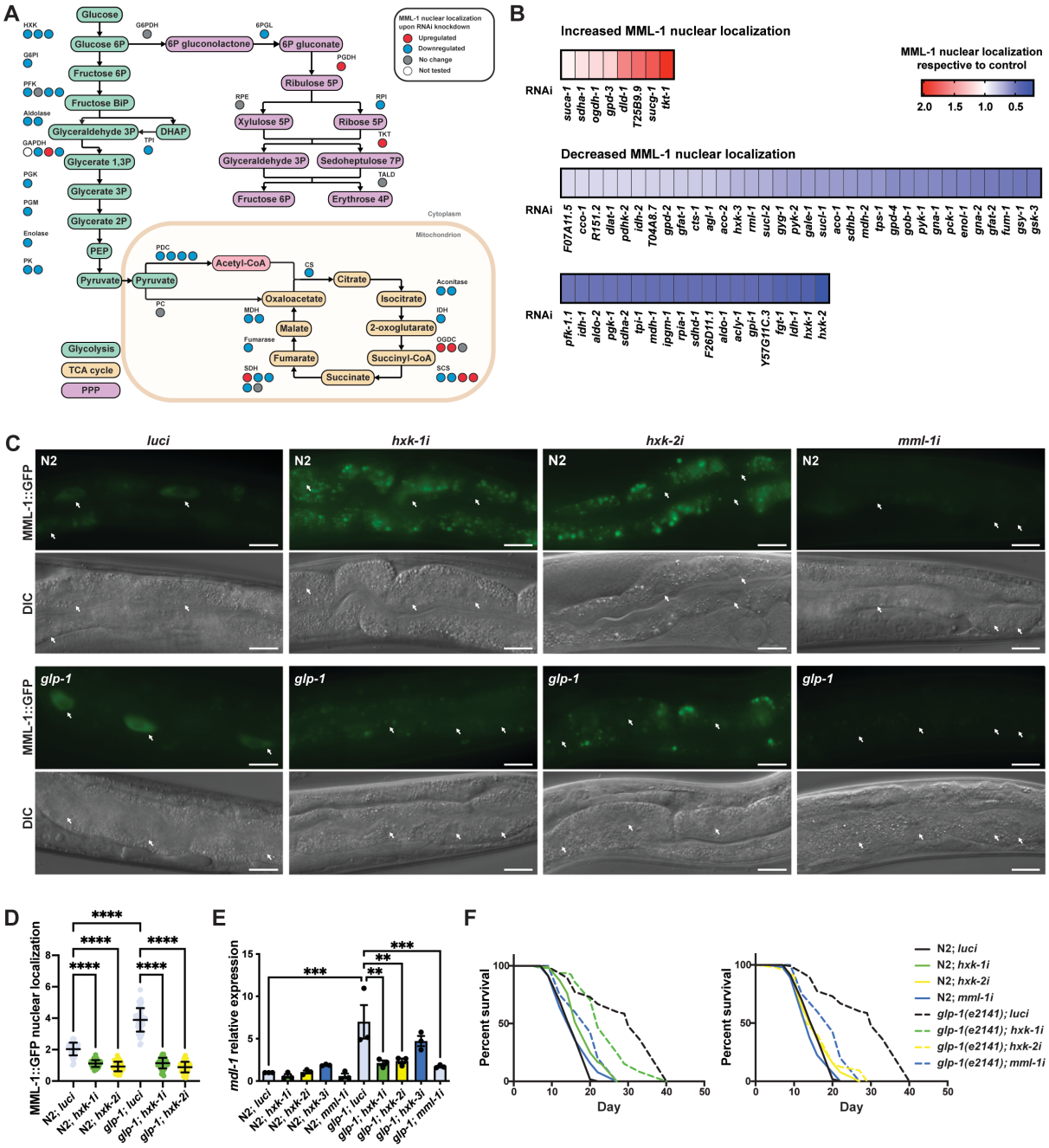

Figure 1. Hexokinases are required for germline longevity through the regulation of MML-1 localization and function. A. Screening for MML-1 regulators upon knockdown of glucose metabolism enzymes. For clarity, we only mapped the candidate genes involved in glycolysis, TCA cycle, and PPP. See **Supplementary Table S1** for a complete list of genes tested. MML-1::GFP nuclear localization was measured in intestinal cells of day one adult worms grown in the RNAi egg-on. Each circle represents one gene encoding an isozyme or subunit of the complex. Circles are color-coded to indicate the increase (red) or decrease (blue) of MML-1::GFP nuclear localization upon knockdown of the enzymes compared to internal *luci* controls. DHAP, dihydroxyacetone phosphate; PEP, phosphoenolpyruvate; TCA cycle,

857 tricarboxylic acid cycle; PPP, pentose phosphate pathway. **B.** Quantification of MML-1 nuclear
858 localization upon knockdown of glucose metabolism genes. Only genes that statistically
859 affected MML-1 nuclear localization compared to the internal *luci* control are depicted
860 ($p<0.05$; N≥2). **C-D.** Representative images (**C**) and quantification (**D**) of MML-1 nuclear
861 localization in wildtype and the germline-less *glp-1(e2141)* longevity background upon
862 knockdown of *luci* (control), *hxk-1i*, *hxk-2i*, and *mml-1i.* MML-1::GFP was quantified in nuclei
863 from intestinal cells (white arrows) in day one adult worms (N=3). Scale bars, 10 μm. **E.**
864 Relative mRNA levels of MML-1 downstream target *mdl-1* in young adult worms measured
865 by qPCR (N=3). **F.** Lifespans of wildtype and *glp-1(e2141)* upon *hxk-1* and *hxk-2* knockdown.
866 Lifespans for *hxk-1* and *hxk-2* knockdown were performed in the same experiment and plotted
867 separately for clarity; therefore, control lifespans are shared between plots. Statistical
868 significance was calculated with *t*-test in **A** and **B,** one-way ANOVA in **D**, two-tailed *t*-test in
869 **E**, and Log-rank (Mantel-Cox) test in **F**. **D** bars represent mean ± SD, and **E** bars represent
870 mean ± SEM.
871

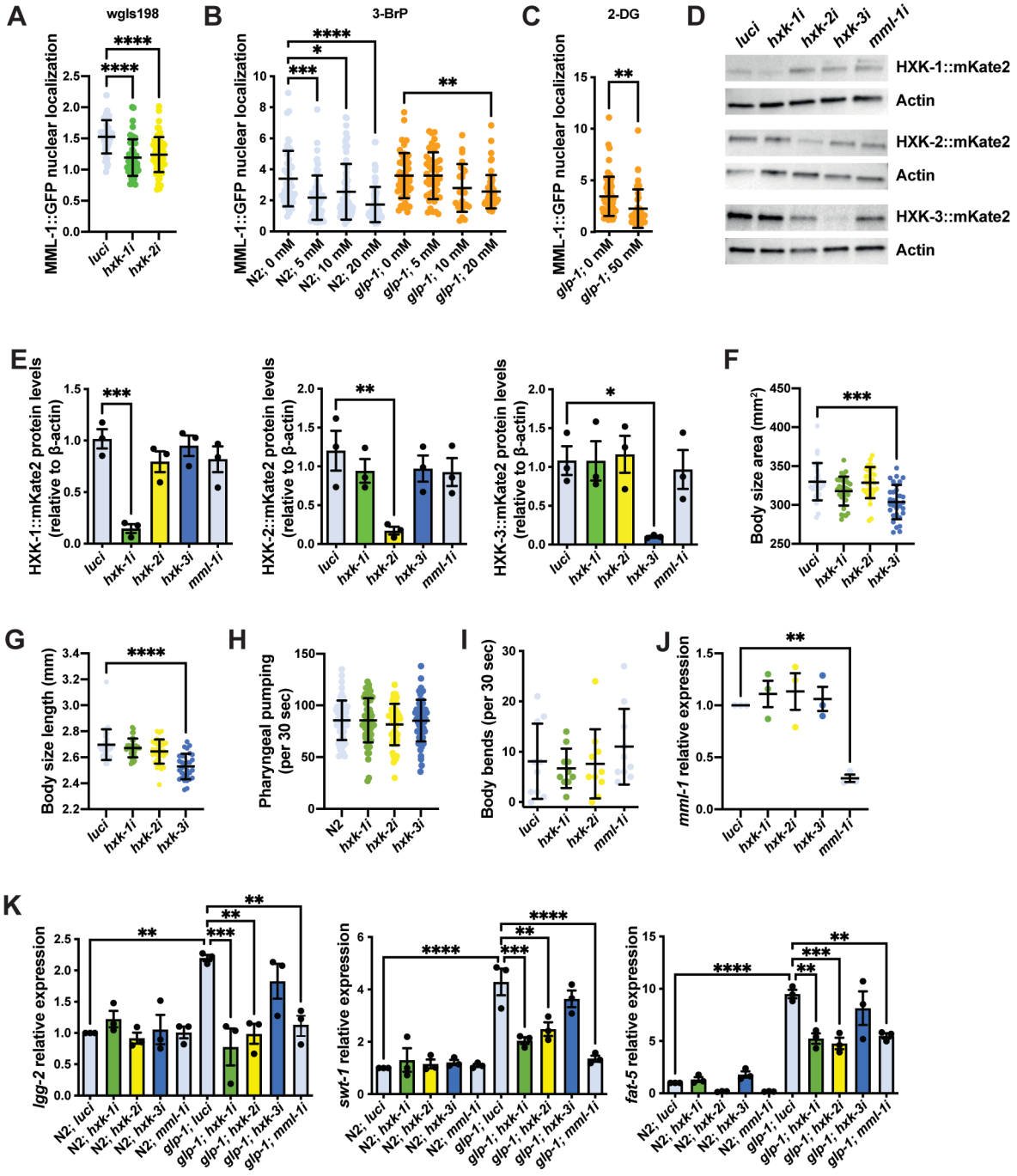

Supplementary Figure 1. Hexokinases regulate MML-1 nuclear localization and transcriptional function. A. MML-1 nuclear localization in the fosmid line wgIs198 was quantified in intestinal cells of day one adult worms using upon *hxk-1* and *hxk-2* knockdown (N=3). **B**. Quantification of MML-1 nuclear localization in intestinal cells of day one adult wildtype and *glp-1(e2141)* worms supplemented with the glycolytic inhibitor 3-bromopyruvate (3-BrP) 5, 10, and 20 mM egg-on (N=2). **C**. Quantification of MML-1 nuclear localization in intestinal cells of day one adult *glp-1(e2141)* worms supplemented with the glycolytic inhibitor 2-deoxy-glucose (2-DG) 50 mM egg-on (N=2). **D-E.** Representative Western blot (**D**) and densitometry analysis (**E**) of hexokinases basal levels under *hxk-1i*, *hxk-2i*, *hxk-3i*, and *mml-1i*.

882 Protein levels were normalized to actin as a loading control (N=3). **F-H.** Measurements of body
883 size area (**F**), length (**G**), and pharyngeal pumping rate (**H**) of day one adult worms grown
884 under hexokinase knockdown (N=3). **I**. Motility assay of day one adult worms grown under
885 hexokinase knockdown (N=2). **J.** Relative *mml-1* mRNA levels under hexokinase knockdown
886 measured by qPCR (N=3). **K.** Relative mRNA expression of MML-1 downstream targets
887 *lgg-2*, *swt-1*, and *fat-5* measured by qPCR (N=3). Statistical significance was calculated with
888 *t*-test in **C** and one-way ANOVA in **A-B** and **E-K**. **A-C** and **F-J** bars represent mean ± SD, and
889 **E** and **K** bars represent mean ± SEM.
890

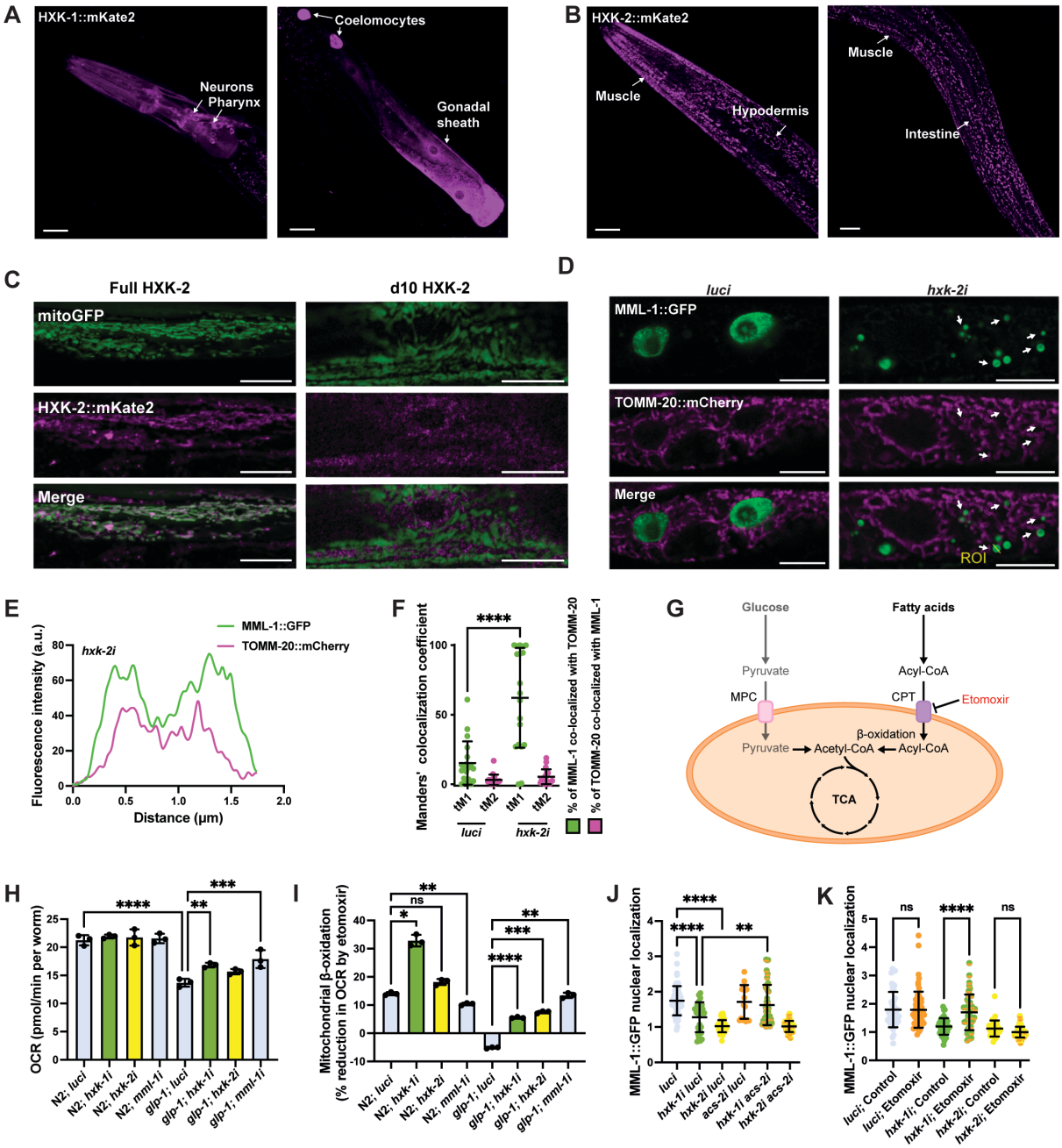

891

892 **Figure 2. Enhanced mitochondrial β-oxidation suppresses MML-1 nuclear localization**
893 **upon *hxk-1* knockdown. A-B.** Tissue expression of HXK-1::mKate2 (**A**) and HXK-2::mKate2
894 (**B**) isozymes. The primary tissues are identified with arrows. Scale bars, 20 μm. **C.**
895 Colocalization of mitochondrial reporter *myo-3p*::mitoGFP with full-length HXK-2::mKate2
896 and d10 HXK-2::mKate2 lacking the first ten residues of the N-terminus. Scale bars, 10 μm.
897 **D.** Representative confocal images of day one adult worms expressing MML-1::GFP and the
898 mitochondrial reporter *ges-1p*::TOMM-20::mCherry under *luci* and *hxk-2i*. Scale bars, 10 μm.
899 **E.** Intensity plot of the region of interest (ROI) from *hxk-2i* (**D**). **F.** Colocalization of
900 MML-1::GFP and TOMM-20::mCherry in *luci* and *hxk-2i*. The colocalization analysis was
901 calculated with the thresholded Mander's colocalization coefficients tM1 (GFP channel) and
902 tM2 (mCherry channel) (N=3). **G.** When glycolysis is reduced, cells rely on fatty acids for
903 energy production. Free fatty acids are activated to acyl-CoA and transported to the
904 mitochondria through the CPT in the mitochondrial outer membrane. The acyl-CoA is then
905 metabolized to generate acetyl-CoA that can enter the TCA cycle to produce energy. MPC,
906 mitochondrial pyruvate carrier; CPT, carnitine palmitoyltransferase. **H-I.** Oxygen consumption
907 rate (OCR) under basal conditions (**H**) and after the addition of the mitochondrial β-oxidation
908 inhibitor etomoxir (**I**). Mitochondrial β-oxidation is calculated as the percentage of decreased
909 OCR after the injection of etomoxir (N=3). **J.** MML-1 nuclear localization of day one adult
910 worms grown with double knockdown of *hxk-1* or *hxk-2* combined *acs-2i* (N=3). **K.** MML-1
911 nuclear localization of day one adult worms grown upon *hxk-1* and *hxk-2* knockdown with
912 supplementation of etomoxir 100 μM egg-on (N=3). Statistical significance was calculated
913 with *t*-test in **F**, and one-way ANOVA in **H-K**. **F** and **J-K** bars represent mean ± SD, **H-I** bars
914 represent mean ± SEM.
915

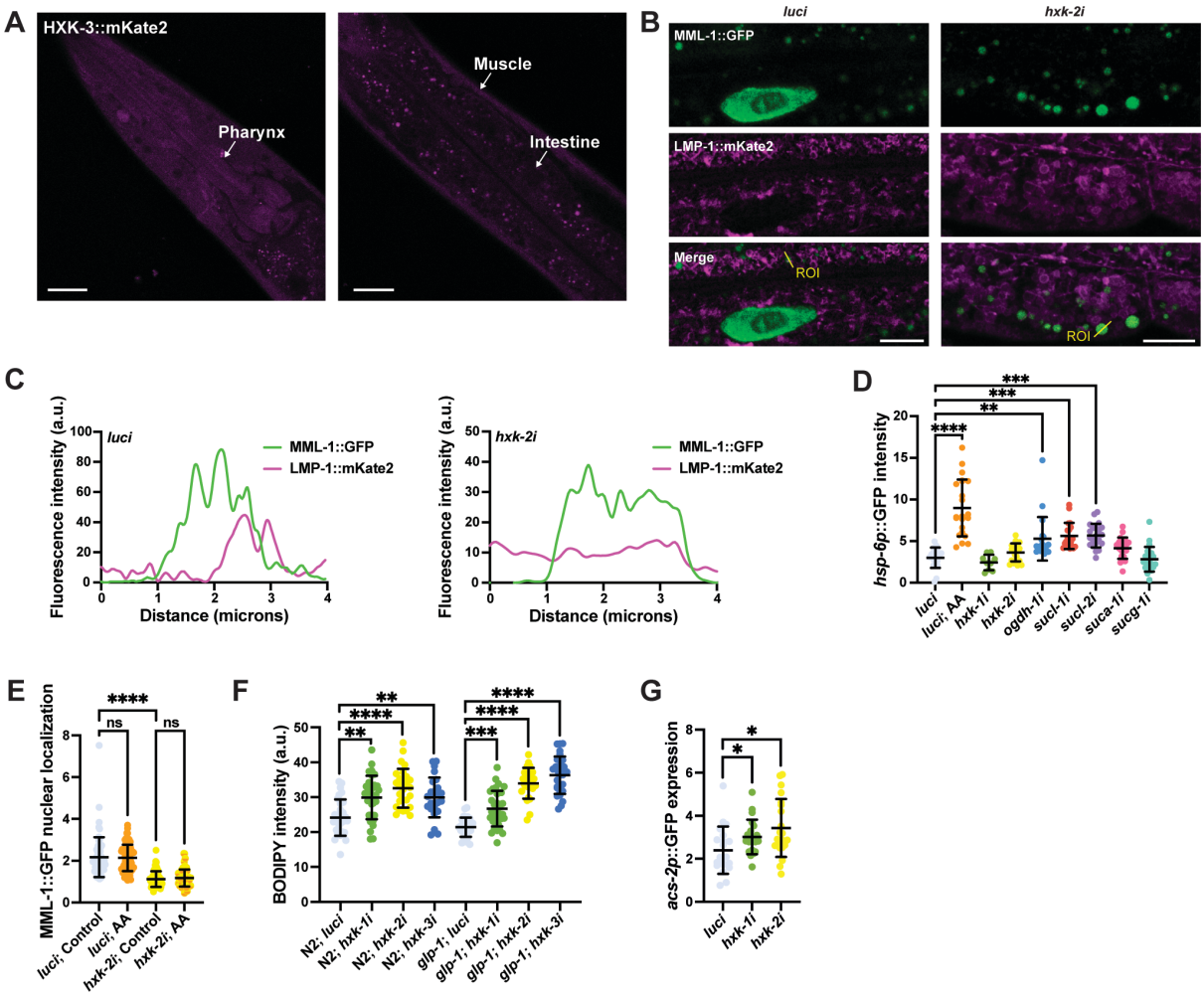

Supplementary Figure 2. MML-1 regulation by glucose metabolism is independent of mitochondrial stress response activation. A. Localization of HXK-3::mKate2 isozyme. The primary tissues are identified with arrows. Scale bars, 20 µm. **B.** Representative confocal images of day one adult worms expressing MML-1::GFP and the lysosome/endosome reporter LMP-1::mKate2 under *luci* and *hxk-2i*. Scale bars, 10 µm. **C.** Intensity plots of the ROIs from **B** (n>10 MML-1 positive puncta per worm). **D.** Quantification of mitochondrial stress response *hsp-6p*::GFP transcriptional reporter upon knockdown of candidate genes regulating MML-1 nuclear localization. Worms were imaged on day one of adulthood. As a positive control for induction of mitochondrial stress, worms were supplemented with antimycin A (AA) 10 µg/mL for 24 h before imaging (N=3). **E.** Quantification of MML-1::GFP nuclear localization of worms grown under *luci* and *hxk-2i* supplemented with AA at the L4 stage, and nuclear localization was measured after 24 h (N=3). **F.** Neutral lipid content was measured on day one of adulthood by feeding worms with C1-BODIPY-C12 egg-on (N=3). **G.** Quantification of day one adult worms expressing the transcriptional reporter *acs-2p*::GFP under hexokinase

knockdown (N=3). Statistical significance was calculated with one-way ANOVA in **D-G**. **D-G** bars represent mean ± SD.

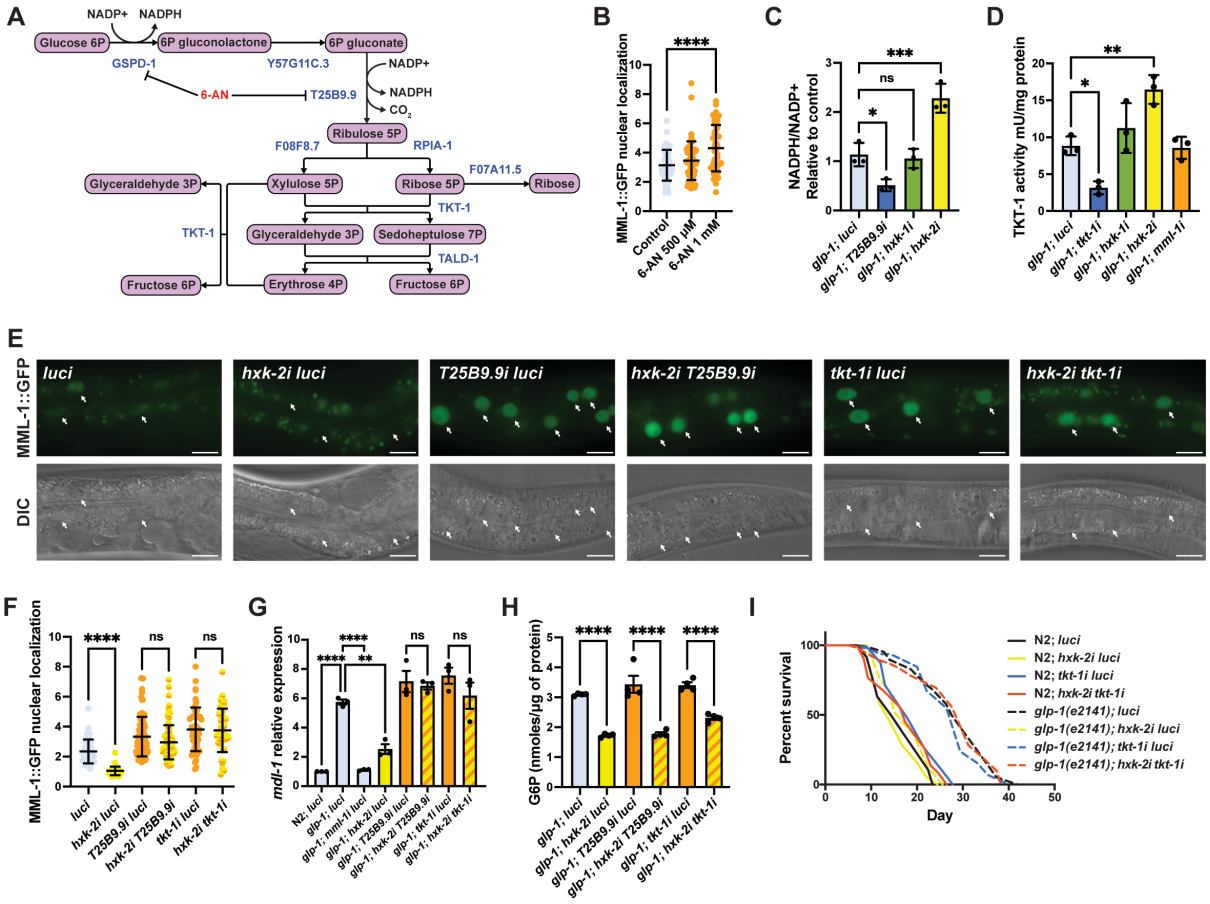

Figure 3. HXK-2 regulates MML-1 localization and function through inhibition of the PPP. A. The PPP is a cytosolic pathway that metabolizes G6P to produce NADPH and ribose-5P, and interconverts 3 to 7 carbon sugars. 6-Aminonicotinamide (6-AN) is a PPP inhibitor that acts on the NADPH-producing enzymes GSPD-1 and T25B9.9. **B.** Quantification of MML-1 nuclear localization of day one adult worms supplemented with 500 µM and 1 mM of 6-AN egg-on (N=3). **C.** Quantification of $NADP^+$ and NADPH levels in day one adult *glp-1(e2141)* worms grown under hexokinase knockdown. *T25B9.9i* was used as a control. Metabolite levels were normalized to total protein concentration (N=3). **D.** Transketolase enzymatic activity assay in day one adult *glp-1(e2141)* worms grown under hexokinase knockdown. *tkt-1i* was used as a control. Activity levels were normalized to total protein concentration (N=3). **E-F.** Representative images (**E**) and quantification (**F**) of MML-1 nuclear localization of day one adult worms upon double knockdown of *hxk-2* with the PPP enzymes *T25B9.9* and *tkt-1* (N=3). **G.** Relative mRNA levels of MML-1 downstream target *mdl-1* in young adult worms upon double knockdown of *hxk-2* in combination with enzymes of the PPP

949 measured by qPCR (N=3). **H.** Quantification of G6P levels relative to total protein measured
950 in day one adult *glp-1(e2141)* upon double knockdown of *hxk-2* in combination with enzymes
951 of the PPP (N=4). **I.** Lifespan analysis of *glp-1(e2141)* with *hxk-2i* and *tkt-1i* single and double
952 knockdowns. Lifespan was performed in the same experiment as **Supplementary Figure 3J**;
953 therefore, control lifespans are shared between plots (N=3). Statistical significance was
954 calculated with a one-way ANOVA test in **B-D** and **F-H**, and Log-rank (Mantel-Cox) test in **I**.
955 **B** and **F** bars represent mean ± SD, **C-D** and **G-H** bars represent mean ± SEM.
956

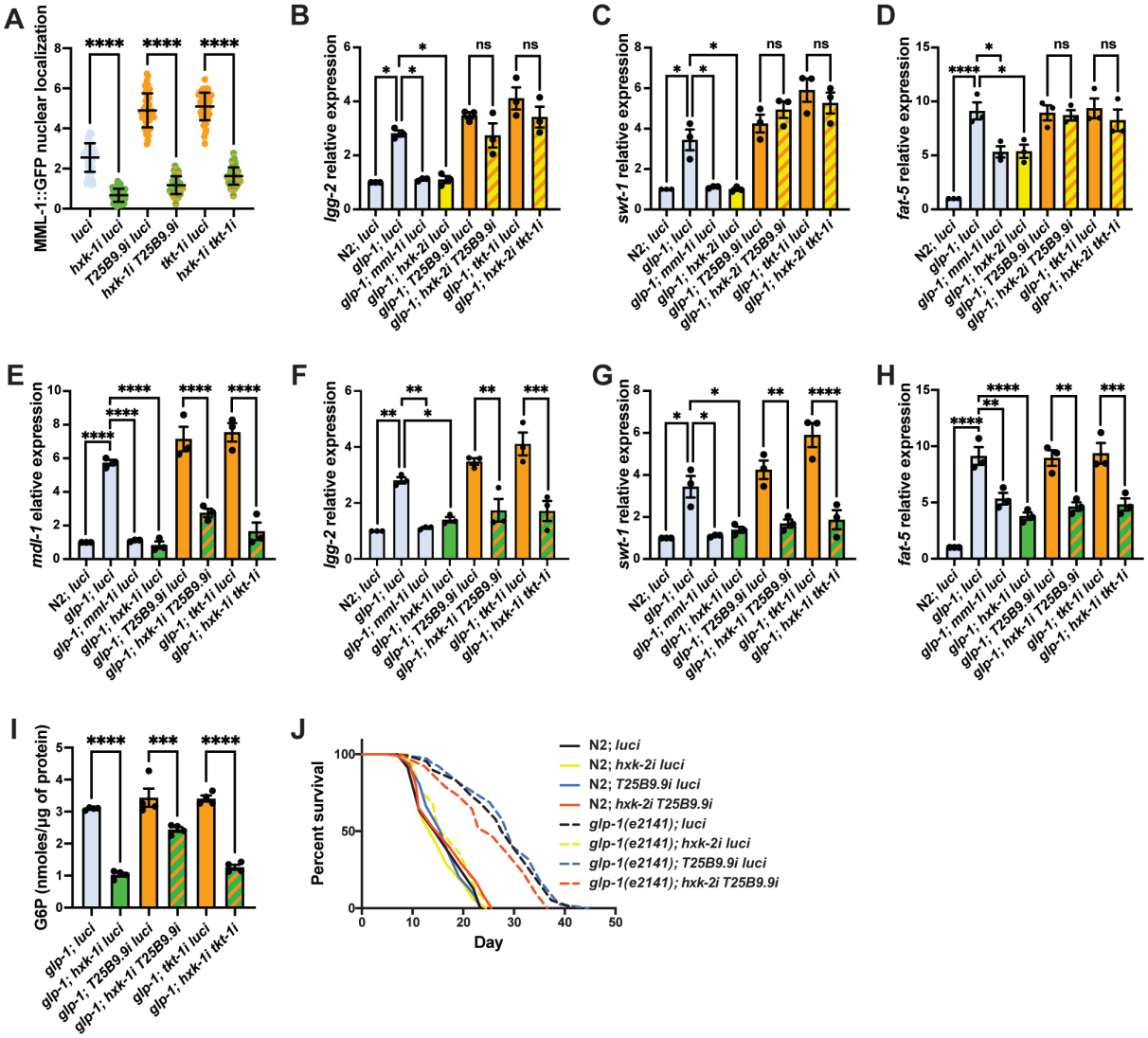

957

958 **Supplementary Figure 3. HXK-1 and HXK-2 regulate MML-1 through parallel or**
959 **independent pathways. A.** MML-1 nuclear localization of day one adult worms upon double
960 knockdown of *hxk-1* with enzymes of the PPP (N=3). **B-D.** Relative mRNA levels of MML-1
961 downstream targets *lgg-2* (**B**), *swt-1* (**C**), and *fat-5* (**D**) in young adult worms with double
962 knockdown of *hxk-2* with enzymes of the PPP measured by qPCR (N=3). **E-H.** Relative mRNA

963 levels of MML-1 downstream targets *mdl-1* (**E**), *lgg-2* (**F**), *swt-1* (**G**), and *fat-5* (**H**) in young
964 adult worms with double knockdown of *hxk-1* with enzymes of the PPP measured by qPCR
965 (N=3). **I**. Quantification of G6P levels relative to total protein measured in day one adult
966 *glp-1(e2141)* worms grown under *hxk-1i* in combination with enzymes from the PPP (N=4). **J.**
967 Lifespan analysis of *glp-1(e2141)* with *hxk-2i* and *T25B9.9i* single and double knockdowns.
968 Lifespan was performed in the same experiment as **Figure 3I**; therefore, control lifespans are
969 shared between plots (N=3). Statistical significance was calculated with a one-way ANOVA
970 test in **A-I**, and Log-rank (Mantel-Cox) test in **J**. **A** bars represent mean ± SD, **B-I** bars
971 represent mean ± SEM.
972

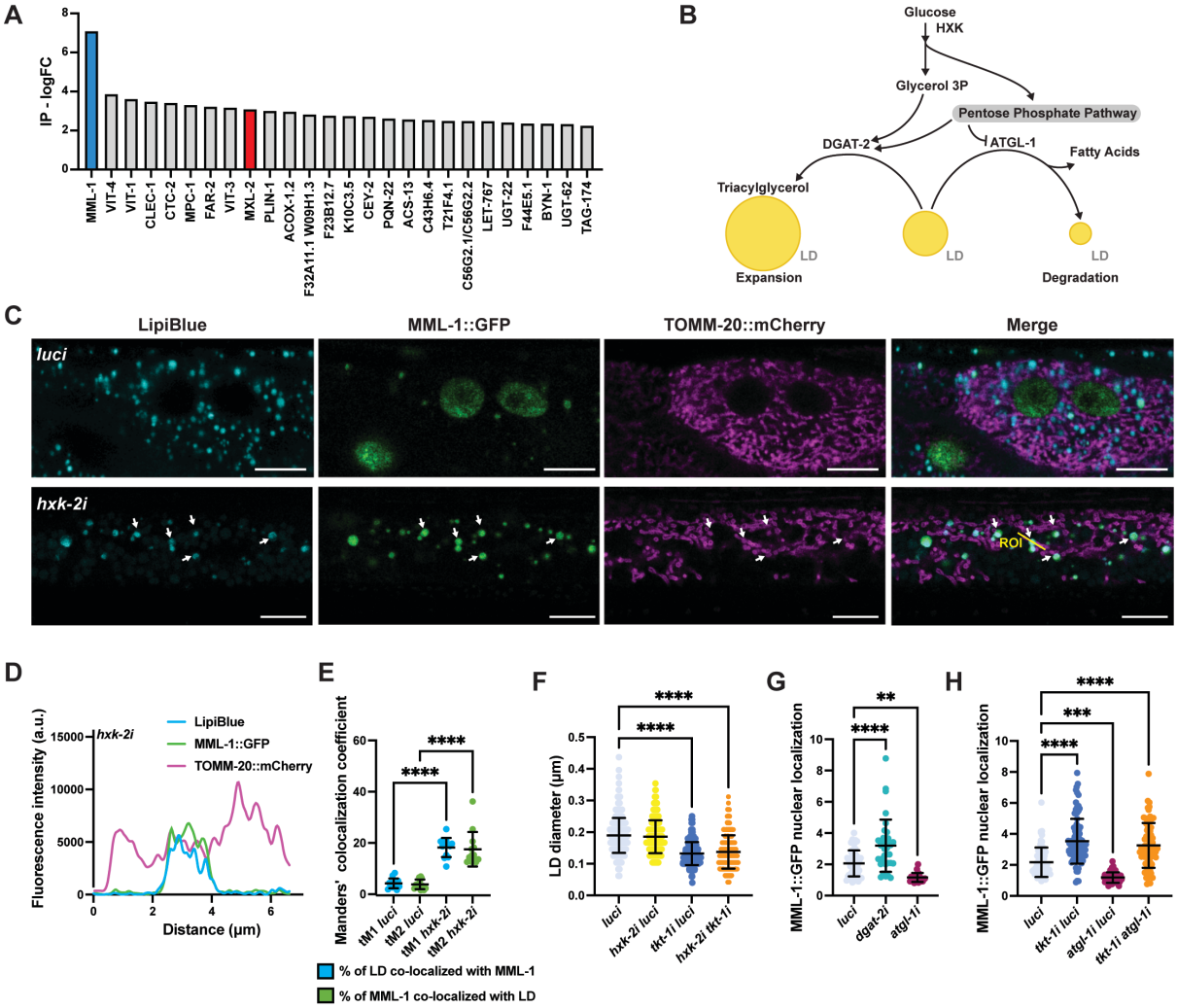

973

974 **Figure 4. *hxk-2* knockdown increases MML-1 colocalization with LD. A.** Anti-FLAG
975 immunoprecipitation (IP) from whole-worm lysates of animals expressing MML-1
976 endogenously tagged with 3xFLAG in wildtype background. IP was analyzed by mass
977 spectrometry (LC-MS/MS). The 25 top candidates co-enriched with MML-1 compared to non-
978 transgenic wildtype control are shown as log FC, including MML-1 (blue) and its established

979 binding partner MXL-2 (red). **B.** Crosstalk between glycolysis, PPP, and lipid droplet (LD)
980 metabolism. On the one hand, LD expansion is favored by increased fatty acid synthesis and
981 subsequent formation of triacylglycerol (TAG) by the diacylglycerol acetyltransferase
982 DGAT-2. On the other hand, LD consumption releases free fatty acids from TAG by the rate-
983 limiting lipase ATGL-1. **C.** Confocal microscopy of day one adult worms expressing
984 MML-1::GFP and the mitochondrial reporter TOMM-20::mCherry stained with the LD dye
985 LipiBlue under *luci* and *hxk-2i* (N=3). Scale bars, 10 μm. **D.** Intensity plot of the region of
986 interest (ROI) from *hxk-2i* (**C**). **E.** Colocalization of MML-1::GFP and LD in *luci* and *hxk-2i*.
987 The colocalization analysis was calculated with the thresholded Mander's colocalization
988 coefficients tM1 (GFP channel) and tM2 (LipiBlue channel) (N=3). **F.** Quantification of LD
989 diameter in day one adult worms expressing the LD reporter PLIN-1::mCherry upon
990 knockdown of *hxk-2* and *tkt-1* (N=3). **G.** Quantification of MML-1 nuclear localization under
991 knockdown of the LD metabolic enzymes *dgat-2* and *atg-1* (N=3). **H.** Quantification of
992 MML-1 nuclear localization upon double knockdown of *tkt-1* and *atgl-1* (N=3). Statistical
993 significance was calculated with a one-way ANOVA test in **E-H**. **E-H** bars represent mean ±
994 SD.
995

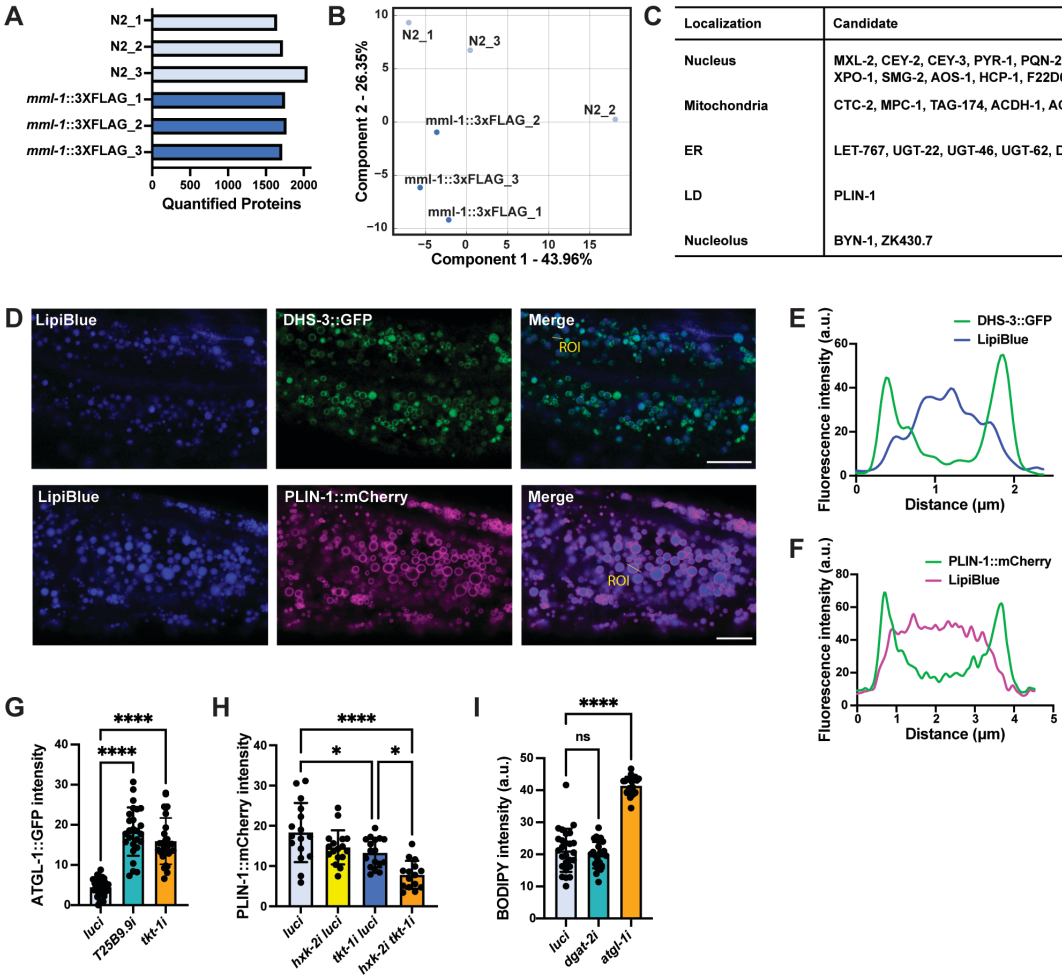

Localization	Candidate
Nucleus	MXL-2, CEY-2, CEY-3, PYR-1, PQN-22, PQN-59, KDP-1, XPO-1, SMG-2, AOS-1, HCP-1, F22D6.2, IFET-1
Mitochondria	CTC-2, MPC-1, TAG-174, ACDH-1, ACS-13
ER	LET-767, UGT-22, UGT-46, UGT-62, DPY-18, ELO-1
LD	PLIN-1
Nucleolus	BYN-1, ZK430.7

Supplementary Figure 4. MML-1 interactome is enriched with proteins from different organelles. A. Quantified proteins in each biological replicate of wildtype and *mml-1::3xFLAG* anti-FLAG immunoprecipitation (IP). **B**. Principal component analysis (PCA) with each biological replicate of the genotypes from proteomics. **C.** Top candidates co-enriched in MML-1::FLAG IP grouped by predicted subcellular localization (uniport.org). **D.** Representative images of day one adult worms expressing the LD proteins DHS-3::GFP and PLIN-1::mCherry reporters grown with the LD dye LipiBlue egg-on. Scale bars, 10 µm. **E-F.** Intensity plots of the marked ROI from **D** showing DHS-3::GFP (**E**) and PLIN-1::mCherry (**F**) colocalization with LipiBlue. **G.** Expression of the ATGL-1::GFP translational reporter measured on day one adult worms grown under *T25B9.9* and *tkt-1* RNAi egg-on (N=3). **H.** Quantification of LD reporter PLIN-1::mCherry intensity in day one adult worms upon knockdown of *hxk-2* and *tkt-1* (N=3). **I.** Quantification of neutral lipid content in day one adult worms supplemented with C1-BODIPY-C12 egg-on under *dgat-2* and *atgl-1* knockdown (N=3). Statistical significance was calculated with a one-way ANOVA test in **G-I**. **G-I** bars represent mean ± SD.

1012

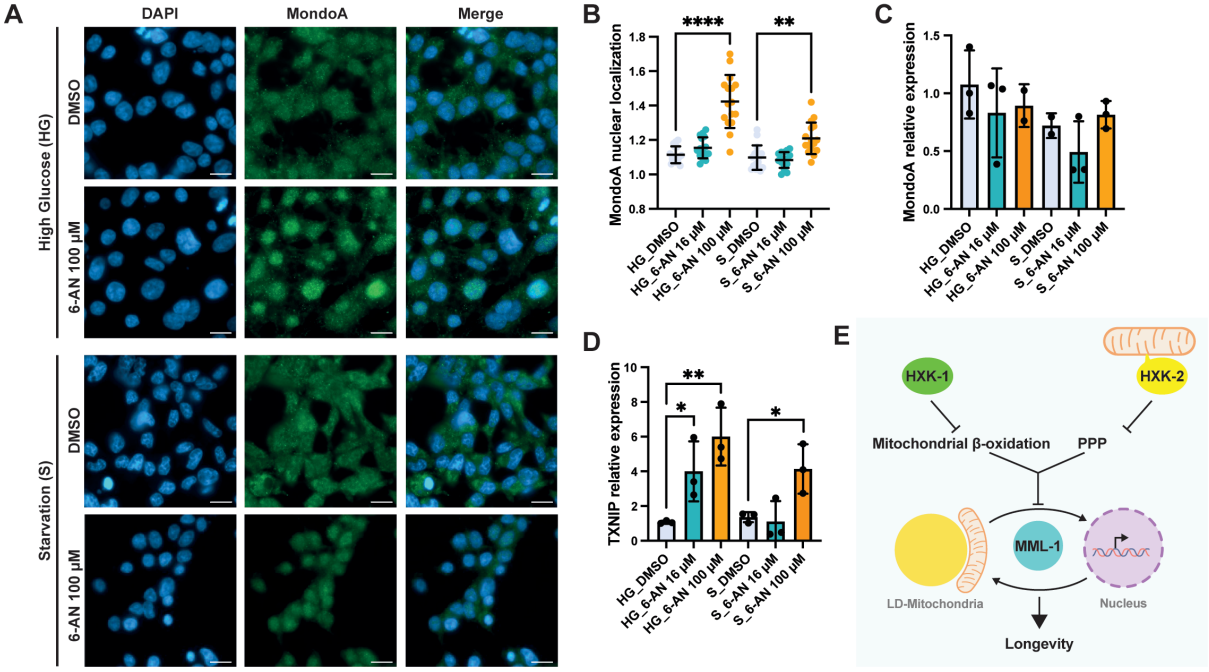

1013

1014 **Figure 5. MondoA localization and transcriptional function is regulated by PPP in**
1015 **HEK293T cells. A.** Immunofluorescence of MondoA in HEK293T cells under high glucose
1016 media (HG) and starvation (S) conditions supplemented with the PPP inhibitor
1017 6-aminonicotinamide (6-AN) 100 μM. Scale bars, 20 μm. **B.** Quantification of MondoA
1018 nuclear localization in HEK293T cells treated with 6-AN 16 and 100 μM under HG and S
1019 conditions (N=3). **C.** Relative mRNA levels of *MondoA* in HEK293T cells treated with 6-AN
1020 16 and 100 μM under HG and S conditions measured by qPCR (N=3). **D.** Relative mRNA
1021 levels of MondoA downstream target *TXNIP* in HEK293T cells treated with 6-AN 16 and 100
1022 μM under HG and S conditions measured by qPCR (N=3). Statistical significance was
1023 calculated with one-way ANOVA in **B-D**. **B** bars represent mean ± SD, **C-D** bars represent
1024 mean ± SEM. **E.** Working model of MML-1 regulation by hexokinases. MML-1 is positively
1025 regulated by HXK-1 and HXK-2 through different downstream mechanisms. Inhibition of the
1026 mitochondrial β-oxidation rescues MML-1 nuclear localization upon *hxk-1i*, while decreasing
1027 enzymes from the PPP rescues MML-1 localization upon *hxk-2i*. These upstream mechanisms
1028 regulate MML-1 subcellular localization between LD-mitochondria and the nucleus, which is
1029 required for the lifespan extension mediated by germ-line loss. PPP, pentose phosphate
1030 pathway; LD, lipid droplet.

1031

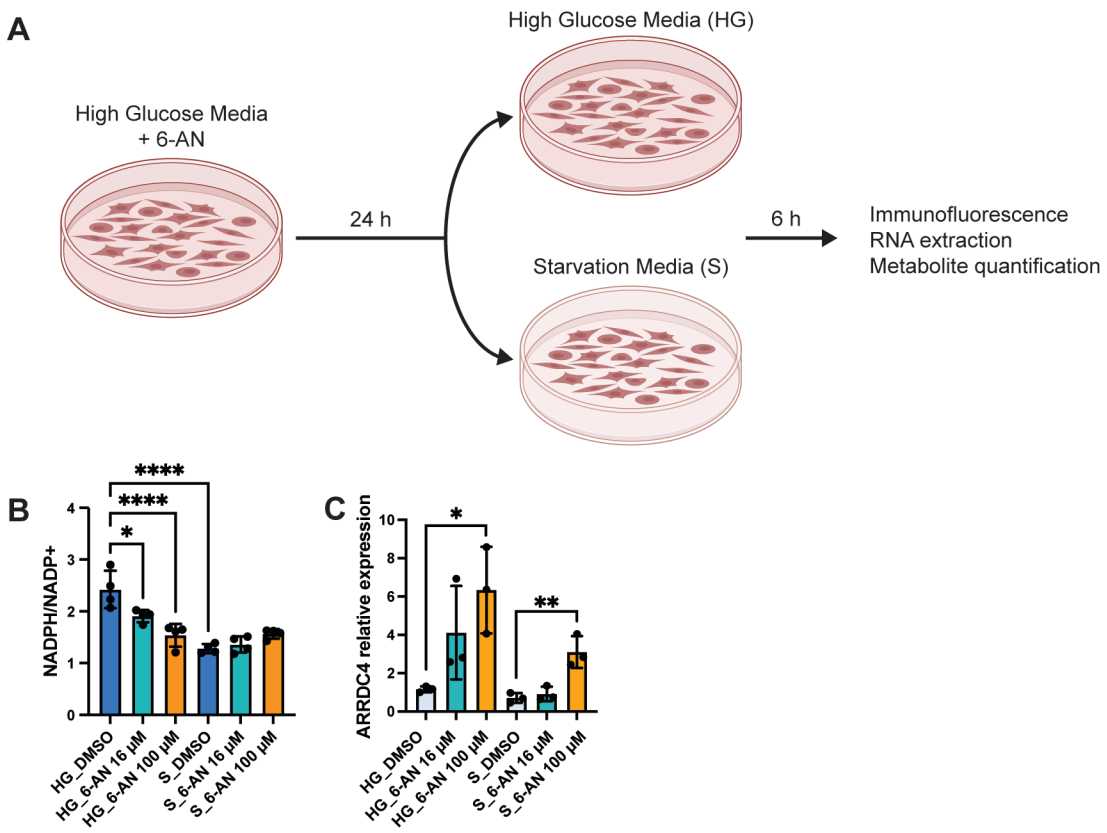

Supplementary Figure 5. Inhibition of PPP NADPH-producing enzymes by 6-AN induces MondoA downstream targets. A. Experimental design for inhibition of the PPP in HEK293T cells. Cells were grown in high glucose media (HG) supplemented with 6-AN for 24 h, and then the media was replaced with either HG or starvation (S) media for 6 h. Cells were collected and used for immunostaining, RNA extraction, and metabolite quantification. **B.** Quantification of $NADP^+$ and NADPH levels in HEK293T cells treated with 6-AN 16 and 100 µM under HG and S conditions (N=3). **C.** Relative mRNA levels of MondoA downstream target *ARRDC4* in HEK293T cells treated with 6-AN 16 and 100 µM under HG and S conditions measured by qPCR (N=3). Statistical significance was calculated with one-way ANOVA in **B-C**. **B-C** bars represent mean ± SEM.

References

Benhamed, F., Denechaud, P. D., Lemoine, M., Robichon, C., Moldes, M., Bertrand-Michel, J., Ratziu, V., Serfaty, L., Housset, C., Capeau, J., Girard, J., Guillou, H., & Postic, C. (2012). The lipogenic transcription factor ChREBP dissociates hepatic steatosis from insulin resistance in mice and humans. *Journal of Clinical Investigation*, *122*(6), 2176–2194. https://doi.org/10.1172/JCI41636

Bennett, C. F., Kwon, J. J., Chen, C., Russell, J., Acosta, K., Burnaevskiy, N., Crane, M. M.,

1051 Bitto, A., Vander Wende, H., Simko, M., Pineda, V., Rossner, R., Wasko, B. M., Choi,
1052 H., Chen, S., Park, S., Jafari, G., Sands, B., Perez Olsen, C., … Kaeberlein, M. (2017).
1053 Transaldolase inhibition impairs mitochondrial respiration and induces a starvation-like
1054 longevity response in Caenorhabditis elegans. In *PLoS Genetics* (Vol. 13, Issue 3).
1055 https://doi.org/10.1371/journal.pgen.1006695
1056 Billin, A. N., Eilers, A. L., Coulter, K. L., Logan, J. S., & Ayer, D. E. (2000). MondoA, a
1057 Novel Basic Helix-Loop-Helix–Leucine Zipper Transcriptional Activator That
1058 Constitutes a Positive Branch of a Max-Like Network. *Molecular and Cellular Biology*,
1059 *20*(23), 8845–8854. https://doi.org/10.1128/mcb.20.23.8845-8854.2000
1060 Bolte, S., & Cordelières, F. P. (2006). A guided tour into subcellular colocalization analysis
1061 in light microscopy. *Journal of Microscopy*, *224*(3), 213–232.
1062 https://doi.org/10.1111/j.1365-2818.2006.01706.x
1063 Boutant, M., Kulkarni, S. S., Joffraud, M., Ratajczak, J., Valera-Alberni, M., Combe, R.,
1064 Zorzano, A., & Cantó, C. (2017). Mfn2 is critical for brown adipose tissue thermogenic
1065 function. *The EMBO Journal*, *36*(11), 1543–1558.
1066 https://doi.org/10.15252/embj.201694914
1067 Bricker, D. K., Taylor, E. B., Schell, J. C., Orsak, T., Boutron, A., Chen, Y.-C., Cox, J. E.,
1068 Cardon, C. M., Van Vranken, J. G., Dephoure, N., Redin, C., Boudina, S., Gygi, S. P.,
1069 Brivet, M., Thummel, C. S., & Rutter, J. (2012). A Mitochondrial Pyruvate Carrier
1070 Required for Pyruvate Uptake in Yeast, Drosophila, and Humans. *Science*, *337*(July),
1071 96–100. https://doi.org/10.1126/science.1218099
1072 Carroll, P. A., Diolaiti, D., McFerrin, L., Gu, H., Djukovic, D., Du, J., Cheng, P. F.,
1073 Anderson, S., Ulrich, M., Hurley, J. B., Raftery, D., Ayer, D. E., & Eisenman, R. N.
1074 (2015). Deregulated Myc Requires MondoA/Mlx for Metabolic Reprogramming and
1075 Tumorigenesis. *Cancer Cell*, *27*(2), 271–285. https://doi.org/10.1016/j.ccell.2014.11.024
1076 Cha-Molstad, H., Saxena, G., Chen, J., & Shalev, A. (2009). Glucose-stimulated expression
1077 of Txnip is mediated by carbohydrate response element-binding protein, p300, and
1078 histone H4 acetylation in pancreatic beta cells. *Journal of Biological Chemistry*,
1079 *284*(25), 16898–16905. https://doi.org/10.1074/jbc.M109.010504
1080 Chi, M. M. Y., Pusateri, M. E., Carter, J. G., Norris, B. J., McDougal, D. B., & Lowry, O. H.
1081 (1987). Enzymatic assays for 2-deoxyglucose and 2-deoxyglucose 6-phosphate.
1082 *Analytical Biochemistry*, *161*(2), 508–513. https://doi.org/10.1016/0003-2697(87)90481-
1083 7
1084 Chin, R. M., Fu, X., Pai, M. Y., Vergnes, L., Hwang, H., Deng, G., Diep, S., Lomenick, B.,

1085 Meli, V. S., Monsalve, G. C., Hu, E., Whelan, S. A., Wang, J. X., Jung, G., Solis, G. M.,
1086 Fazlollahi, F., Kaweeteerawat, C., Quach, A., Nili, M., … Huang, J. (2014). The
1087 metabolite α-ketoglutarate extends lifespan by inhibiting ATP synthase and TOR.
1088 *Nature*, *510*(7505), 397–401. https://doi.org/10.1038/nature13264
1089 Clancy, D. J., Gems, D., Harshman, L. G., Oldham, S., Stocker, H., Hafen, E., Leevers, S. J.,
1090 & Partridge, L. (2001). Extension of life-span by loss of CHICO, a Drosophila insulin
1091 receptor substrate protein. *Science*, *292*(5514), 104–106.
1092 https://doi.org/10.1126/science.1057991
1093 Cox, J., Hein, M. Y., Luber, C. A., Paron, I., Nagaraj, N., & Mann, M. (2014). Accurate
1094 proteome-wide label-free quantification by delayed normalization and maximal peptide
1095 ratio extraction, termed MaxLFQ. *Molecular and Cellular Proteomics*, *13*(9), 2513–
1096 2526. https://doi.org/10.1074/mcp.M113.031591
1097 Cox, J., & Mann, M. (2008). MaxQuant enables high peptide identification rates,
1098 individualized p.p.b.-range mass accuracies and proteome-wide protein quantification.
1099 *Nature Biotechnology*, *26*(12), 1367–1372. https://doi.org/10.1038/nbt.1511
1100 Dalziel, K., & Londesborough, J. C. (1968). The mechanisms of reductive carboxylation
1101 reactions: Carbon dioxide or bicarbonate as substrate of nicotinamide-adenine
1102 dinucleotide phosphate-linked isocitrate dehydrogenase and malic enzyme. *The*
1103 *Biochemical Journal*, *110*(2), 223–230. https://doi.org/10.1042/bj1100223
1104 Denechaud, P. D., Dentin, R., Girard, J., & Postic, C. (2008). Role of ChREBP in hepatic
1105 steatosis and insulin resistance. *FEBS Letters*, *582*(1), 68–73.
1106 https://doi.org/10.1016/j.febslet.2007.07.084
1107 Du, S., & Zheng, H. (2021). Role of FoxO transcription factors in aging and age-related
1108 metabolic and neurodegenerative diseases. *Cell and Bioscience*, *11*(1), 1–17.
1109 https://doi.org/10.1186/s13578-021-00700-7
1110 Fischer, F., Grigolon, G., Benner, C., & Ristow, M. (2022). Evolutionarily Conserved
1111 Transcription Factors As Regulators of Longevity and Targets for Geroprotection.
1112 *Physiological Reviews*, *102*(3), 1449–1494. https://doi.org/10.1152/physrev.00017.2021
1113 Gerisch, B., & Antebi, A. (2004). Hormonal signals produced by DAF-9/cytochrome P450
1114 regulate C. elegans dauer diapause in response to environmental cues. *Development*,
1115 *131*(8), 1765–1776. https://doi.org/10.1242/dev.01068
1116 Gerisch, B., Weitzel, C., Kober-Eisermann, C., Rottiers, V., & Antebi, A. (2001). A
1117 Hormonal Signaling Pathway Influencing C. elegans Metabolism, Reproductive
1118 Development, and Life Span. *Developmental Cell*, *1*(6), 841–851.

https://doi.org/10.1016/S1534-5807(01)00085-5

Ghasemi, A., Aghajani, H., Fallah, S., Assadi, M., & Seifi, M. (2015). C771G (His241Gln) polymorphism of MLXIPL Gene, TG levels and coronary artery disease: A case control study. *Anatolian Journal of Cardiology*, *15*(1), 8–12. https://doi.org/10.5152/akd.2014.5135

Gordaliza-Alaguero, I., Cantó, C., & Zorzano, A. (2019). Metabolic implications of organelle–mitochondria communication. *EMBO Reports*, *20*(9), 1–27. https://doi.org/10.15252/embr.201947928

Gottlob, K., Majewski, N., Kennedy, S., Kandel, E., Robey, R. B., & Hay, N. (2001). Inhibition of early apoptotic events by Akt/PKB is dependent on the first committed step of glycolysis and mitochondrial hexokinase. *Genes and Development*, *15*(11), 1406–1418. https://doi.org/10.1101/gad.889901

Green, C. L., Lamming, D. W., & Fontana, L. (2021). Molecular mechanisms of dietary restriction promoting health and longevity. *Nature Reviews Molecular Cell Biology*, *0123456789*. https://doi.org/10.1038/s41580-021-00411-4

Hutter, H., & Suh, J. (2016). GExplore 1.4: An expanded web interface for queries on Caenorhabditis elegans protein and gene function . *Worm*, *5*(4), e1234659. https://doi.org/10.1080/21624054.2016.1234659

Iizuka, K., Miller, B., & Uyeda, K. (2006). Deficiency of carbohydrate-activated transcription factor ChREBP prevents obesity and improves plasma glucose control in leptin-deficient (ob/ob) mice. *American Journal of Physiology - Endocrinology and Metabolism*, *291*(2), 358–364. https://doi.org/10.1152/ajpendo.00027.2006

Ishii, S., Iizuka, K., Miller, B. C., & Uyeda, K. (2004). Carbohydrate response element binding protein directly promotes lipogenic enzyme gene transcription. *Proceedings of the National Academy of Sciences of the United States of America*, *101*(44), 15597–15602. https://doi.org/10.1073/pnas.0405238101

John, S., Weiss, J. N., & Ribalet, B. (2011). Subcellular localization of hexokinases I and II directs the metabolic fate of glucose. *PLoS ONE*, *6*(3). https://doi.org/10.1371/journal.pone.0017674

Johnson, D. W., Llop, J. R., Farrell, S. F., Yuan, J., Stolzenburg, L. R., & Samuelson, A. V. (2014). The Caenorhabditis elegans Myc-Mondo/Mad Complexes Integrate Diverse Longevity Signals. *PLoS Genetics*, *10*(4). https://doi.org/10.1371/journal.pgen.1004278

Ju, H. Q., Lin, J. F., Tian, T., Xie, D., & Xu, R. H. (2020). NADPH homeostasis in cancer: functions, mechanisms and therapeutic implications. *Signal Transduction and Targeted*

1153 *Therapy*, *5*(1), 1–12. https://doi.org/10.1038/s41392-020-00326-0
1154 Kaadige, M. R., Looper, R. E., Kamalanaadhan, S., & Ayer, D. E. (2009). Glutamine-
1155 dependent anapleurosis dictates glucose uptake and cell growth by regulating MondoA
1156 transcriptional activity. *Proceedings of the National Academy of Sciences of the United*
1157 *States of America*, *106*(35), 14878–14883. https://doi.org/10.1073/pnas.0901221106
1158 Kamath, R. S., & Ahringer, J. (2003). Genome-wide RNAi screening in Caenorhabditis
1159 elegans. *Methods*, *30*(4), 313–321. https://doi.org/10.1016/S1046-2023(03)00050-1
1160 Kennedy, B. K., & Lamming, D. W. (2016). The Mechanistic Target of Rapamycin: The
1161 Grand ConducTOR of Metabolism and Aging. *Cell Metabolism*, *23*(6), 990–1003.
1162 https://doi.org/10.1016/j.cmet.2016.05.009
1163 Koopman, M., Michels, H., Dancy, B. M., Kamble, R., Mouchiroud, L., Auwerx, J., Nollen,
1164 E. A. A., & Houtkooper, R. H. (2016). A screening-based platform for the assessment of
1165 cellular respiration in Caenorhabditis elegans. *Nature Protocols*, *11*(10), 1798–1816.
1166 https://doi.org/10.1038/nprot.2016.106
1167 Krahmer, N., Najafi, B., Schueder, F., Quagliarini, F., Steger, M., Seitz, S., Kasper, R.,
1168 Salinas, F., Cox, J., Uhlenhaut, N. H., Walther, T. C., Jungmann, R., Zeigerer, A.,
1169 Borner, G. H. H., & Mann, M. (2018). Organellar Proteomics and Phospho-Proteomics
1170 Reveal Subcellular Reorganization in Diet-Induced Hepatic Steatosis. *Developmental*
1171 *Cell*, *47*(2), 205-221.e7. https://doi.org/10.1016/j.devcel.2018.09.017
1172 Lapierre, L. R., De Magalhaes Filho, C. D., McQuary, P. R., Chu, C. C., Visvikis, O., Chang,
1173 J. T., Gelino, S., Ong, B., Davis, A. E., Irazoqui, J. E., Dillin, A., & Hansen, M. (2013).
1174 The TFEB orthologue HLH-30 regulates autophagy and modulates longevity in
1175 Caenorhabditis elegans. *Nature Communications*, *4*.
1176 https://doi.org/10.1038/ncomms3267
1177 Lee, J. H., Kong, J., Jang, J. Y., Han, J. S., Ji, Y., Lee, J., & Kim, J. B. (2014). Lipid Droplet
1178 Protein LID-1 Mediates ATGL-1-Dependent Lipolysis during Fasting in Caenorhabditis
1179 elegans. *Molecular and Cellular Biology*, *34*(22), 4165–4176.
1180 https://doi.org/10.1128/mcb.00722-14
1181 Leigh-Brown, S., Enriquez, J. A., & Odom, D. T. (2010). Nuclear transcription factors in
1182 mammalian mitochondria. *Genome Biology*, *11*(7), 1–9. https://doi.org/10.1186/gb-
1183 2010-11-7-215
1184 Li, F., Wang, Y., Zeller, K. I., Potter, J. J., Wonsey, D. R., O'Donnell, K. A., Kim, J.,
1185 Yustein, J. T., Lee, L. A., & Dang, C. V. (2005). Myc Stimulates Nuclearly Encoded
1186 Mitochondrial Genes and Mitochondrial Biogenesis. *Molecular and Cellular Biology*,

1187 *25*(14), 6225–6234. https://doi.org/10.1128/mcb.25.14.6225-6234.2005
1188 Lindén, M., Gellerfors, P., & Dean Nelson, B. (1982). Pore protein and the hexokinase-
1189 binding protein from the outer membrane of rat liver mitochondria are identical. *FEBS*
1190 *Letters*, *141*(2), 189–192. https://doi.org/10.1016/0014-5793(82)80044-6
1191 Ma, L., Robinson, L. N., & Towle, H. C. (2006). ChREBP·Mlx is the principal mediator of
1192 glucose-induced gene expression in the liver. *Journal of Biological Chemistry*, *281*(39),
1193 28721–28730. https://doi.org/10.1074/jbc.M601576200
1194 Marchenko, N. D., Wolff, S., Erster, S., Becker, K., & Moll, U. M. (2007).
1195 Monoubiquitylation promotes mitochondrial p53 translocation. *EMBO Journal*, *26*(4),
1196 923–934. https://doi.org/10.1038/sj.emboj.7601560
1197 Marinov, G. K., Wang, Y. E., Chan, D., & Wold, B. J. (2014). Evidence for site-specific
1198 occupancy of the mitochondrial genome by nuclear transcription factors. *PLoS ONE*,
1199 *9*(1), 1–24. https://doi.org/10.1371/journal.pone.0084713
1200 Massari, M. E., & Murre, C. (2000). *Helix-Loop-Helix Proteins: Regulators of Transcription*
1201 *in Eucaryotic*. *20*(2), 429–440. https://doi.org/10.1128/mcb.20.2.429-440.2000
1202 Mejhert, N., Kuruvilla, L., Gabriel, K. R., Elliott, S. D., Guie, M. A., Wang, H., Lai, Z. W.,
1203 Lane, E. A., Christiano, R., Danial, N. N., Farese, R. V., & Walther, T. C. (2020).
1204 Partitioning of MLX-Family Transcription Factors to Lipid Droplets Regulates
1205 Metabolic Gene Expression. *Molecular Cell*, *77*(6), 1251-1264.e9.
1206 https://doi.org/10.1016/j.molcel.2020.01.014
1207 Motola, D. L., Cummins, C. L., Rottiers, V., Sharma, K. K., Li, T., Li, Y., Suino-Powell, K.,
1208 Xu, H. E., Auchus, R. J., Antebi, A., & Mangelsdorf, D. J. (2006). Identification of
1209 Ligands for DAF-12 that Govern Dauer Formation and Reproduction in C. elegans. *Cell*,
1210 *124*(6), 1209–1223. https://doi.org/10.1016/j.cell.2006.01.037
1211 Mutlu, A. S., Gao, S. M., Zhang, H., & Wang, M. C. (2020). Olfactory specificity regulates
1212 lipid metabolism through neuroendocrine signaling in Caenorhabditis elegans. *Nature*
1213 *Communications*, *11*(1), 1–15. https://doi.org/10.1038/s41467-020-15296-8
1214 Nakamura, S., Karalay, Ö., Jäger, P. S., Horikawa, M., Klein, C., Nakamura, K., Latza, C.,
1215 Templer, S. E., Dieterich, C., & Antebi, A. (2016). Mondo complexes regulate TFEB
1216 via TOR inhibition to promote longevity in response to gonadal signals. *Nature*
1217 *Communications*, *7*. https://doi.org/10.1038/ncomms10944
1218 Orlandi, I., Coppola, D. P., & Vai, M. (2014). Rewiring yeast acetate metabolism through
1219 mpc1 loss of function leads to mitochondrial damage and decreases chronological
1220 lifespan. *Microbial Cell*, *1*(12), 393–405. https://doi.org/10.15698/mic2014.12.178

1221 Owen, O. E., Kalhan, S. C., & Hanson, R. W. (2002). The key role of anaplerosis and
1222 cataplerosis for citric acid cycle function. *Journal of Biological Chemistry*, *277*(34),
1223 30409–30412. https://doi.org/10.1074/jbc.R200006200
1224 Papsdorf, K., Miklas, J. W., Hosseini, A., Cabruja, M., Morrow, C. S., Savini, M., Yu, Y.,
1225 Silva-garcía, C. G., Haseley, N. R., Murphy, L. M., Yao, P., Launoit, E. De, Dixon, S. J.,
1226 Snyder, M. P., Wang, M. C., Mair, W. B., & Brunet, A. (2023). Lipid droplets and
1227 peroxisomes are co-regulated to drive lifespan extension in response to mono-
1228 unsaturated fatty acids. *Nature Cell Biology*. https://doi.org/10.1038/s41556-023-01136-
1229 6
1230 Pastorino, J. G., Shulga, N., & Hoek, J. B. (2002). Mitochondrial binding of hexokinase II
1231 inhibits Bax-induced cytochrome c release and apoptosis. *Journal of Biological*
1232 *Chemistry*, *277*(9), 7610–7618. https://doi.org/10.1074/jbc.M109950200
1233 Penkov, S., Kaptan, D., Erkut, C., Sarov, M., Mende, F., & Kurzchalia, T. V. (2015).
1234 Integration of carbohydrate metabolism and redox state controls dauer larva formation in
1235 Caenorhabditis elegans. *Nature Communications*, *6*.
1236 https://doi.org/10.1038/ncomms9060
1237 Pickett, C. L., Breen, K. T., & Ayer, D. E. (2007). A C. elegans Myc-like network cooperates
1238 with semaphorin and Wnt signaling pathways to control cell migration. *Developmental*
1239 *Biology*, *310*(2), 226–239. https://doi.org/10.1016/j.ydbio.2007.07.034
1240 Postic, C., Dentin, R., Denechaud, P. D., & Girard, J. (2007). ChREBP, a transcriptional
1241 regulator of glucose and lipid metabolism. *Annual Review of Nutrition*, *27*, 179–192.
1242 https://doi.org/10.1146/annurev.nutr.27.061406.093618
1243 R Core Team. (2017). *R: A language and environment for statistical computing* (3.4.3). R
1244 Foundation for Statistical Computing. https://www.r-project.org/
1245 Ralser, M., Wamelink, M. M., Struys, E. A., Joppich, C., Krobitsch, S., Jakobs, C., &
1246 Lehrach, H. (2008). A catabolic block does not sufficiently explain how 2-deoxy-D-
1247 glucose inhibits cell growth. *Proceedings of the National Academy of Sciences of the*
1248 *United States of America*, *105*(46), 17807–17811.
1249 https://doi.org/10.1073/pnas.0803090105
1250 Ramachandran, P. V., Savini, M., Folick, A. K., Hu, K., Masand, R., Graham, B. H., &
1251 Wang, M. C. (2019). Lysosomal Signaling Promotes Longevity by Adjusting
1252 Mitochondrial Activity. *Developmental Cell*, *48*(5), 685-696.e5.
1253 https://doi.org/10.1016/j.devcel.2018.12.022
1254 Rambold, A. S., Cohen, S., & Lippincott-Schwartz, J. (2015). Fatty acid trafficking in starved

1255 cells: Regulation by lipid droplet lipolysis, autophagy, and mitochondrial fusion
1256 dynamics. *Developmental Cell*, *32*(6), 678–692.
1257 https://doi.org/10.1016/j.devcel.2015.01.029
1258 Richards, P., Ourabah, S., Montagne, J., Burnol, A. F., Postic, C., & Guilmeau, S. (2017).
1259 MondoA/ChREBP: The usual suspects of transcriptional glucose sensing; Implication in
1260 pathophysiology. *Metabolism: Clinical and Experimental*, *70*, 133–151.
1261 https://doi.org/10.1016/j.metabol.2017.01.033
1262 Ritchie, M. E., Phipson, B., Wu, D., Hu, Y., Law, C. W., Shi, W., & Smyth, G. K. (2015).
1263 limma powers differential expression analyses for RNA-sequencing and microarray
1264 studies. *Nucleic Acids Research*, *43*(7), e47. https://doi.org/10.1093/nar/gkv007
1265 Roberts, D. J., Tan-Sah, V. P., Ding, E. Y., Smith, J. M., & Miyamoto, S. (2014).
1266 Hexokinase-II Positively Regulates Glucose Starvation-Induced Autophagy through
1267 TORC1 Inhibition. *Molecular Cell*, *53*(4), 521–533.
1268 https://doi.org/10.1016/j.molcel.2013.12.019
1269 Rual, J. F., Ceron, J., Koreth, J., Hao, T., Nicot, A. S., Hirozane-Kishikawa, T., Vandenhaute,
1270 J., Orkin, S. H., Hill, D. E., van den Heuvel, S., & Vidal, M. (2004). Toward improving
1271 Caenorhabditis elegans phenome mapping with an ORFeome-based RNAi library.
1272 *Genome Research*, *14*(10 B), 2162–2168. https://doi.org/10.1101/gr.2505604
1273 Sans, C. L., Satterwhite, D. J., Stoltzman, C. A., Breen, K. T., & Ayer, D. E. (2006).
1274 MondoA-Mlx Heterodimers Are Candidate Sensors of Cellular Energy Status:
1275 Mitochondrial Localization and Direct Regulation of Glycolysis. *Molecular and*
1276 *Cellular Biology*, *26*(13), 4863–4871. https://doi.org/10.1128/mcb.00657-05
1277 Selman, C., Lingard, S., Choudhury, A. I., Batterham, R. L., Claret, M., Clements, M.,
1278 Ramadani, F., Okkenhaug, K., Schuster, E., Blanc, E., Piper, M. D., Al-Qassab, H.,
1279 Speakman, J. R., Carmignac, D., Robinson, I. C. A., Thornton, J. M., Gems, D.,
1280 Partridge, L., & Withers, D. J. (2008). Evidence for lifespan extension and delayed age–
1281 related biomarkers in insulin receptor substrate 1 null mice. *The FASEB Journal*, *22*(3),
1282 807–818. https://doi.org/10.1096/fj.07-9261com
1283 Stoltzman, C. A., Kaadige, M. R., Peterson, C. W., & Ayer, D. E. (2011). MondoA senses
1284 non-glucose sugars: Regulation of thioredoxin-interacting protein (TXNIP) and the
1285 hexose transport curb. *Journal of Biological Chemistry*, *286*(44), 38027–38034.
1286 https://doi.org/10.1074/jbc.M111.275503
1287 Stoltzman, C. A., Peterson, C. W., Breen, K. T., Muoio, D. M., Billin, A. N., & Ayer, D. E.
1288 (2008). Glucose sensing by MondoA:Mlx complexes: A role for hexokinases and direct

regulation of thioredoxin-interacting protein expression. *Proceedings of the National Academy of Sciences of the United States of America*, *105*(19), 6912–6917. https://doi.org/10.1073/pnas.0712199105

Sui, D., & Wilson, J. E. (1997). Structural determinants for the intracellular localization of the isozymes of mammalian hexokinase: Intracellular localization of fusion constructs incorporating structural elements from the hexokinase isozymes and the green fluorescent protein. *Archives of Biochemistry and Biophysics*, *345*(1), 111–125. https://doi.org/10.1006/abbi.1997.0241

Tatenaka, Y., Kato, H., Ishiyama, M., Sasamoto, K., Shiga, M., Nishitoh, H., & Ueno, Y. (2019). Monitoring Lipid Droplet Dynamics in Living Cells by Using Fluorescent Probes. *Biochemistry*, *58*(6), 499–503. https://doi.org/10.1021/acs.biochem.8b01071

Tong, X., Zhao, F., Mancuso, A., Gruber, J. J., & Thompson, C. B. (2009). The glucose-responsive transcription factor ChREBP contributes to glucose-dependent anabolic synthesis and cell proliferation. *Proceedings of the National Academy of Sciences of the United States of America*, *106*(51), 21660–21665. https://doi.org/10.1073/pnas.0911316106

Van Gilst, M. R., Hadjivassiliou, H., & Yamamoto, K. R. (2005). A Caenorhabditis elegans nutrient response system partially dependent on nuclear receptor NHR-49. *Proceedings of the National Academy of Sciences of the United States of America*, *102*(38), 13496–13501. https://doi.org/10.1073/pnas.0506234102

Vrablik, T. L., Petyuk, V. A., Larson, E. M., Smith, R. D., & Watts, J. L. (2015). Lipidomic and proteomic analysis of Caenorhabditis elegans lipid droplets and identification of ACS-4 as a lipid droplet-associated protein. *Biochimica et Biophysica Acta - Molecular and Cell Biology of Lipids*, *1851*(10), 1337–1345. https://doi.org/10.1016/j.bbalip.2015.06.004

Wang, M. C., O'Rourke, E. J., & Ruvkun, G. (2008). Fat metabolism links germline stem cells and longevity in C. elegans. *Science*, *322*(5903), 957–960. https://doi.org/10.1126/science.1162011

Wilde, B. R., Ye, Z., Lim, T. Y., & Ayer, D. E. (2019). Cellular acidosis triggers human mondoa transcriptional activity by driving mitochondrial atp production. *ELife*, *8*, 1–25. https://doi.org/10.7554/eLife.40199

Wilson, J. E. (2003). Isozymes of mammalian hexokinase: Structure, subcellular localization and metabolic function. *Journal of Experimental Biology*, *206*(12), 2049–2057. https://doi.org/10.1242/jeb.00241

Wolf, A. J., Reyes, C. N., Liang, W., Becker, C., Shimada, K., Wheeler, M. L., Cho, H. C., Popescu, N. I., Coggeshall, K. M., Arditi, M., & Underhill, D. M. (2016). Hexokinase Is an Innate Immune Receptor for the Detection of Bacterial Peptidoglycan. *Cell*, *166*(3), 624–636. https://doi.org/10.1016/j.cell.2016.05.076

Yamamoto-Imoto, H., Minami, S., Shioda, T., Yamashita, Y., Sakai, S., Maeda, S., Yamamoto, T., Oki, S., Takashima, M., Yamamuro, T., Yanagawa, K., Edahiro, R., Iwatani, M., So, M., Tokumura, A., Abe, T., Imamura, R., Nonomura, N., Okada, Y., … Yoshimori, T. (2022). Age-associated decline of MondoA drives cellular senescence through impaired autophagy and mitochondrial homeostasis. *Cell Reports*, *38*(9), 110444. https://doi.org/10.1016/j.celrep.2022.110444

Yamashita, H., Takenoshita, M., Sakurai, M., Bruick, R. K., Henzel, W. J., Shillinglaw, W., Arnot, D., & Uyeda, K. (2001). A glucose-responsive transcription factor that regulates carbohydrate metabolism in the liver. *Proceedings of the National Academy of Sciences of the United States of America*, *98*(16), 9116–9121. https://doi.org/10.1073/pnas.161284298

Yamawaki, T. M., Berman, J. R., Suchanek-Kavipurapu, M., McCormick, M., Gaglia, M. M., Lee, S. J., & Kenyon, C. (2010). The somatic reproductive tissues of C. elegans promote longevity through steroid hormone signaling. *PLoS Biology*, *8*(8), 45–46. https://doi.org/10.1371/journal.pbio.1000468

Zhang, Y., Lanjuin, A., Chowdhury, S. R., Mistry, M., Silva-García, C. G., Weir, H. J., Chia-Lin, L., Escoubas, C. C., Tabakovic, E., & Mair, W. B. (2019). Neuronal TORC1 modulates longevity via ampk and cell nonautonomous regulation of mitochondrial dynamics in C. Elegans. *ELife*, *8*, 1–24. https://doi.org/10.7554/eLife.49158